Available online at www.sciencedirect.com

ScienceDirect

Geochimica et Cosmochimica Acta 223 (2018) 279–299

Geochimica et Cosmochimica Acta

www.elsevier.com/locate/gca

Unraveling multiple phases of sulfur cycling during the alteration of ancient ultramafic oceanic lithosphere

Esther M. Schwarzenbach [a,b,*], Benjamin C. Gill [b], David T. Johnston [c]

[a] Institute of Geological Sciences, Freie Universität Berlin, 12249 Berlin, Germany
[b] Department of Geosciences, Virginia Tech, 4044 Derring Hall, Blacksburg, VA 24061, USA
[c] Department of Earth and Planetary Sciences, Harvard University, 302 Hoffman Lab, Cambridge MA 02138, United States

Received 25 August 2017; accepted in revised form 8 December 2017; available online 14 December 2017

Abstract

Ultramafic-hosted hydrothermal systems – characterized by ongoing serpentinization reactions – exert an important influence on the global sulfur cycle. Extensive water-rock interaction causes elemental exchange between seawater and the oceanic lithosphere, effectively removing sulfate from seawater through both abiogenic and biogenic processes. Here, we use bulk rock multiple sulfur isotope signatures (^{32}S, ^{33}S, ^{34}S) and *in situ* sulfide analyses together with petrographic observations to track the sulfur cycling processes and the hydrothermal evolution of ancient peridotite-hosted hydrothermal systems. We investigate serpentinized peridotites from the Northern Apennine ophiolite in Italy and the Santa Elena ophiolite in Costa Rica and compare those with the Iberian Margin (Ocean Drilling Program (ODP) Leg 149 and 173) and the 15°20′N Fracture Zone along the Mid-Atlantic Ridge (ODP Leg 209).

In situ measurements of sulfides in the Northern Apennine serpentinites preserve a large range in $\delta^{34}S_{sulfide}$ of −33.8 to +13.3‰ with significant heterogeneities within single sulfide grains and depending on mineralogy. Detailed mineralogical investigation and comparison with bulk rock $\Delta^{33}S_{sulfide}$ and *in situ* $\delta^{34}S_{sulfide}$ data implies a thermal evolution of the system from high temperatures (~350 °C) that allowed thermochemical sulfate reduction and input of hydrothermal sulfide to lower temperatures (<120 °C) that permitted microbial activity. The change in temperature regime is locally preserved in individual samples and correlates with the progressive uplift and exposure of mantle rock associated with detachment faulting along a mid-ocean ridge spreading center. The Santa Elena peridotites preserve distinct signatures for fluid circulation at high temperatures with both closed system thermochemical sulfate reduction and input of mafic-derived sulfur. In addition, the peridotites provide strong evidence that low Ca^{2+} concentrations in peridotite-hosted systems can limit sulfate removal during anhydrite precipitation at temperatures above 150 °C. This may play a central role for the availability of sulfate to microbial communities within these systems. Overall, the combined application of *in situ* and bulk rock multiple sulfur isotope measurements with petrographic observations allows us to resolve the different episodes of sulfur cycling during alteration of the oceanic lithosphere and the temporal changes between abiogenic and biogenic processes that control the sulfur cycling in these systems.

1. INTRODUCTION

The global sulfur cycle is largely controlled by the dynamic interaction between seawater, oceanic lithosphere, and microbial communities. Alteration of ultramafic oceanic lithosphere proceeds through serpentinization reactions

* Corresponding author at: Institute of Geological Sciences, Freie Universität Berlin, Malteserstr. 74-100, 12249 Berlin, Germany.
E-mail address: esther.schwarzenbach@fu-berlin.de (E.M. Schwarzenbach).

https://doi.org/10.1016/j.gca.2017.12.006
0016-7037/

to form serpentine, magnetite, brucite, talc, amphibole, and hydrogen (Moody, 1976; Frost and Beard, 2007; Andreani et al., 2007; Bach et al., 2004, 2006; Beard et al., 2009; Schwarzenbach et al., 2016a) and initiates an extensive chemical exchange between water and rock (e.g., Alt et al., 2013; Früh-Green et al., 2004). These reactions modify the ocean chemistry and the chemical and petrophysical properties of the oceanic lithosphere (Christensen et al., 2005; Escartin et al., 1997, 2001; Früh-Green et al., 2004; Snow and Dick, 1995). They facilitate the transfer of sulfur between the surficial, exogenic cycle to the longer-timescale endogenic cycle and make serpentinization an important control on the evolution of the global sulfur budgets (e.g., Alt et al., 2013). In particular, alteration of the ultramafic oceanic lithosphere is associated with various abiogenic sulfur cycling reactions that occur over a range of temperatures including sulfate incorporation into mineral phases and thermochemical sulfate reduction to sulfide (Alt et al., 2007; Alt and Shanks, 1998, 2003; Delacour et al., 2008a, 2008b; Schwarzenbach et al., 2012, 2016b). In addition, hydrogen production during serpentinization provides an energy source for chemosynthetic microbial communities that utilize sulfur. Chimney structures at active ultramafic-hosted systems host sulfur metabolizing and methanogenic microbes (Brazelton et al., 2011, 2006; Schrenk et al., 2013, 2004), whereas the serpentinized basement retains direct (e.g., from biomarkers) and indirect (carbon and sulfur isotopic) evidence for microbial activity (e.g., Alt et al., 2013; Klein et al., 2015). Because of this serpentinization environments recently gained increasing interest for the study of early life on Earth as well as other planetary bodies and icy moons (Russell et al., 2010; Schulte et al., 2006; Vance et al., 2016).

Due to the differential utilization of sulfur during abiogenic and biogenic reactions, sulfur isotope signatures are an ideal tool to track the interplay between mineral reactions, microbial activity, and fluids during oceanic lithosphere alteration. Until relatively recently, sulfur isotope studies have focused predominantly on the analyses of the traditional $^{34}S/^{32}S$ ratios as a tracer for Earth systems processes, while multiple sulfur isotope studies that also analyze the less abundant isotopes ^{33}S and ^{36}S have mostly concentrated on meteorites (e.g., Farquhar et al., 2000b, 2000c) and Archaean sedimentary rocks (Farquhar et al., 2000a; Ono et al., 2003; Ueno et al., 2008) that preserve a distinct isotopic signal of mass-independent sulfur fractionation (as reviewed by Johnston (2011)). However, increased analytical precision has allowed the use of multiple sulfur isotopes in the study of high temperature equilibrium, diffusion, and biological processes that follow mass-dependent fractionation pathways (e.g., Farquhar et al., 2003; Johnston et al., 2005; Labidi et al., 2016). Recent studies have used multiple sulfur isotope signatures to unravel the complexity of processes prevailing during alteration of oceanic crust (McDermott et al., 2015; Oeser et al., 2012; Ono et al., 2012, 2007; Peters et al., 2011; Rouxel et al., 2008). These studies have allowed insight into the mixing ratios between seawater- and basaltic-derived sulfur and non-equilibrium isotopic exchange mechanisms in high-temperature vent systems; identify the effects of sediment-covered hydrothermal systems on fluid chemistry; and recognize biogenic signatures and estimate metabolic rates in basaltic oceanic crust (McDermott et al., 2015; Ono et al., 2007; Peters et al., 2010; Rouxel et al., 2008). Further, $^{34}S/^{32}S$ and $^{33}S/^{32}S$ ratios have been used to indicate closed versus open system microbial sulfate reduction at the serpentinites located on the Iberian Margin (Ono et al., 2012).

The alteration of the ancient oceanic lithosphere involves numerous processes as the rock experiences multiple episodes of hydrothermal circulation under varying temperature conditions. This complex hydrothermal evolution is obscured when analyzing the bulk rock isotopic signatures (Schwarzenbach et al., 2012). In contrast, *in situ* determination of isotopic signatures can be used to resolve microscale isotopic heterogeneities found within particular sulfur bearing phases and can inform on the reconstruction of this complex alteration history (e.g., Rouxel et al., 2008).

In order to unravel the diversity of processes in the sulfur cycle found within peridotite-hosted systems we investigated variably serpentinized peridotites from two ophiolite sequences – the N. Apennine ophiolite in Italy and the Santa Elena ophiolite in Costa Rica. These systems are then compared with serpentinites recovered by ocean drilling to assess the evolution of the sulfur cycle during the alteration of these peridotite-hosted hydrothermal systems. Here, we combine bulk rock multiple sulfur isotope signatures (^{32}S, ^{33}S, ^{34}S) and *in situ* $^{34}S/^{32}S$ ratios of individual sulfide mineral grains with mineralogical and petrographic observations. The combination of these analyses allows us to provide new constraints on temporal changes in fluid chemistry (e.g., redox conditions) and sources, and the temporal sequence of abiogenic and biogenic reactions that process sulfur within these systems.

2. SAMPLES AND GEOLOGICAL BACKGROUND

This study focuses on variably serpentinized peridotites from two ophiolite sequences: the Northern Apennine ophiolite in Italy and the Santa Elena ophiolite in Costa Rica. In addition, we present data from oceanic serpentinites recovered during the Ocean Drilling Program (ODP): (1) samples from the Iberian Margin: ODP Leg 149 Site 897 (Holes 897C and 897D) and ODP Leg 173 Holes 1068A and 1070A, and (2) samples from three drill sites near the Mid-Atlantic Ridge (MAR) 15′20°N Fracture Zone (FZ); ODP Leg 209 Holes 1268A, 1272A, and 1274A (Fig. 1). These data are also compared to multiple sulfur isotope data from ODP Sites 897 and 1268 previously analyzed by Ono et al. (2012). These ODP samples record the large range of conditions found in peridotite-hosted hydrothermal systems and provide a framework to compare the sulfur isotope signatures preserved in the ophiolite sequences.

2.1. The Northern Apennine ophiolite

The ophiolite sequence in the N. Apennine in Italy is comprised of strongly serpentinized peridotites and gabbroic sequences. Occasionally basaltic lava flows and massive sulfide deposits lay atop serpentinized peridotite

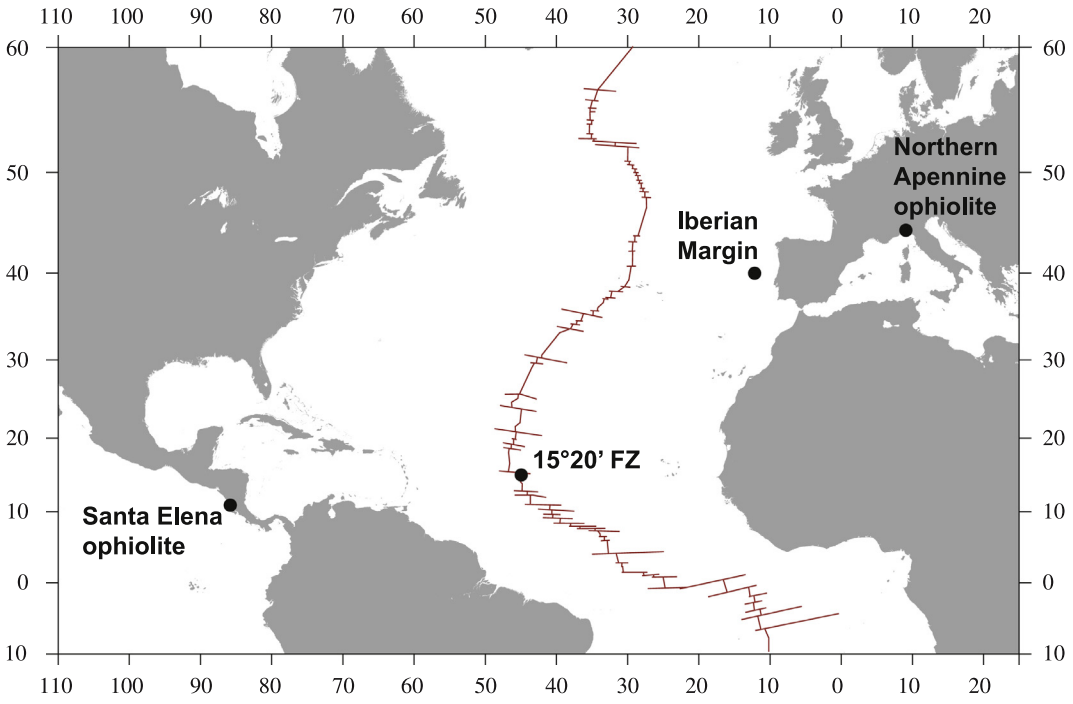

Fig. 1. Location of the investigated samples, which include variably calcite-veined and serpentinized peridotites from the Northern Apennine ophiolite in Italy, the Iberian Margin, the 15°20′N Fracture Zone (FZ) along the Mid-Atlantic Ridge, and the Santa Elena ophiolite in Costa Rica.

(Garuti et al., 2008). The samples studied here were collected in the same quarries as those presented in Schwarzenbach et al. (2012, 2013). They consist of entirely serpentinized peridotites and contain an increasing abundance of carbonate veining with decreasing depth within the ophiolite. The sequences of oceanic lithosphere exposed in the N. Apennine formed during the divergence of the European and Adriatic plates in the Jurassic when detachment faulting along a slow-spreading ridge resulted in the exposure of mantle rocks and initiated serpentinization and extensive carbonate-veining (Abbate et al., 1980; Lemoine, 1980). Serpentinization temperatures for this sequence have been estimated at ~150–240 °C and carbonate formation temperatures at ~50–150 °C (Barrett and Friedrichsen, 1989; Schwarzenbach et al., 2013). Previous investigation of the sulfur geochemistry suggests a multistage history of sulfur cycling involving microbial sulfate reduction, hydrothermal sulfide addition and later leaching of sulfide under relatively oxidizing conditions (Schwarzenbach et al., 2012). While evidence of past high temperature fluid circulation has been documented in serpentinites from several localities in the vicinity of the studied quarries (reflected by the presence of hydrothermal sulfide deposits), an overall evolution of the system to lower temperature processes has been suggested (Alt et al., 2012).

2.2. The Santa Elena ophiolite

The Santa Elena ophiolite is located on the northwest coast of Costa Rica and is comprised of predominantly ultramafic lithologies with local intrusions of mafic dikes. This sequence of oceanic lithosphere has geochemical similarities to slow-spreading mid-ocean ridge environments (Escuder-Viruete et al., 2015; Madrigal et al., 2015). Emplacement of the mafic dikes has been dated to 131–116 Ma (Madrigal et al., 2015). The peridotites are variably serpentinized (30–100%) with estimated serpentinization temperatures <250 °C (Schwarzenbach et al., 2014). The sulfide and metal mineralogies imply highly reducing conditions and the local introduction of high temperature fluids that produced Cu-bearing sulfides and metals (Schwarzenbach et al., 2014). Following obduction, interaction of meteoric water with the ultramafic rocks has continued to serpentinize and alter the peridotites (Sanchez-Murillo et al., 2014; Schwarzenbach et al., 2016b). For an additional discussion of the sulfur geochemistry and mineralogy of the Santa Elena samples we refer the reader to Schwarzenbach et al. (2014) and Schwarzenbach et al. (2016b).

2.3. The Iberian Margin

The Iberian Margin has been described as typical magma-poor rifted margin (Boillot et al., 1980; Sawyer et al., 1994; Whitmarsh et al., 1998). Rifting occurred in the Early Cretaceous and resulted in the opening of the North Atlantic and the development of the Mid-Atlantic Ridge (Boillot et al., 1980). Serpentinization took place as mantle rocks were exposed to seawater just before initiation of seafloor spreading resulting in the formation of strongly calcite-veined serpentinites (Sawyer et al., 1994). Previous studies of the Iberian Margin indicate extensive microbial

sulfate reduction as evidenced by $\delta^{34}S$ values of sulfides as low as −45.1‰ (Alt and Shanks, 1998; Schwarzenbach et al., 2012) and distinct $^{33}S/^{32}S$ ratios (Ono et al., 2012). At Site 897, the dominant sulfide mineralogy transitions from pyrite to pyrrhotite with increasing depth below the seafloor, implying the transition to more reducing conditions, and the sulfur isotope signatures suggest closed system microbial sulfate reduction (Alt and Shanks, 1998; Ono et al., 2012). Here, microbial sulfate reduction was most likely permitted by low serpentinization temperature (<100–150 °C) (Schwarzenbach et al., 2013) and the reducing conditions created by serpentinization (Alt and Shanks, 1998).

2.4. The 15°20′N Fracture Zone along the Mid-Atlantic Ridge

Variably serpentinized peridotites have been recovered from several drill sites during ODP Leg 209 along the MAR, where detachment faulting exposed mantle rocks near the 15°20′N FZ (Kelemen et al., 2007). Previous studies provide evidence for melt depletion followed by extensive serpentinization and localized talc-alteration, which is reflected by Si-metasomatism (Bach et al., 2004; Harvey et al., 2014; Paulick et al., 2006). Oxygen and sulfur isotope signatures suggest low serpentinization temperatures (<150 °C estimated from $\delta^{18}O$ in silicate phases) and microbially produced sulfide at Sites 1272 and 1274 (Alt et al., 2007). At Sites 1268 and 1271, high temperature (~250–350 °C) fluid circulation is associated with the addition of sulfide from hydrothermal fluids, which is reflected in both $^{34}S/^{32}S$ and $^{33}S/^{32}S$ ratios (Alt et al., 2007; Ono et al., 2012). High-temperature venting is also found in the nearby location of the Logatchev hydrothermal field, where acidic, metal-rich fluids vent at temperatures of 300–350 °C from black smoker type chimneys that sit on a basement dominated by ultramafic rocks (Lackschewitz et al., 2005; Petersen et al., 2009; Schmidt et al., 2007).

3. MATERIALS AND METHODS

3.1. Analytical methods

3.1.1. Bulk rock sulfur analyses

To prepare bulk rock powders the outermost rind of the rock samples were cut away to eliminate the potentially weathered or the surficially contaminated portion of the rock. The samples were crushed to gravel size using a jaw crusher and then powdered in a ball mill. Sulfur extraction of the acid volatile sulfide (AVS; representing single bound sulfide such as pyrrhotite) and chromium reducible sulfide (CRS; representing double bound sulfide such as pyrite) was carried out on the bulk rock powders utilizing a modified version of the methods of Tuttle et al. (1986) and Canfield et al. (1986). AVS was extracted by reacting 20–25 g of bulk rock powder with 6 N HCl in a N_2-atmosphere. Tin(II) chlorite was added to the sample to reduce any present Fe^{3+} to Fe^{2+} and prevent oxidation of H_2S to elemental sulfur (Tuttle et al., 1986). The residual powder was then reacted with an acidified $CrCl_2$ solution to extract the chromium-reducible sulfide. In both cases, the released H_2S was precipitated as ZnS in a zinc acetate solution and then converted to Ag_2S through reaction with 0.1 M $AgNO_3$. The sulfate fraction was recovered by reacting the HCl solution from the AVS extraction with $BaCl_2$ to form $BaSO_4$. The AVS, CRS, and sulfate extracts were analyzed on a Vario ISOTOPE elemental analyzer (EA) at the Department of Geosciences at Virginia Tech to determine the $\delta^{34}S$ (see definitions below) of the AVS, CRS and sulfate. During the analytical sessions where these samples were measured, the international sulfide (Ag_2S) standards IAEA-S-1 ($\delta^{34}S = -0.3‰$ (Robinson, 1995; Coplen and Krouse, 1998; Stickler et al., 1995), average measured $-0.14 \pm 0.1‰$), IAEA-S-2 ($\delta^{34}S = +22.7 \pm 0.2‰$ (Robinson, 1995; Stickler et al., 1995), average measured $+22.60 \pm 0.08‰$) and IAEA-S-3 ($\delta^{34}S = -32.3 \pm 0.2‰$ (Robinson, 1995; Stickler et al., 1995), average measured $-32.37 \pm 0.08‰$) and the sulfate ($BaSO_4$) standards IAEA-SO-5 ($\delta^{34}S = +0.5 \pm 0.2‰$ (Halas and Szaran, 2001), average measured $+0.8 \pm 0.15‰$), IAEA-SO-6 ($\delta^{34}S = -34.1 \pm 0.2‰$ (Halas and Szaran, 2001), average measured $-34.3 \pm 0.15‰$), and NBS127 ($\delta^{34}S = +20.3 \pm 0.4‰$ (Halas and Szaran, 2001), average measured $+20.1 \pm 0.15‰$) were also analyzed. Reproducibility was better than ≤0.4‰ (2σ) for all sulfur analyses and the relative precision of sulfur contents is within 3%.

A subset of sulfide extracts (AVS and CRS fraction, see Table 1) was subsequently processed on the fluorination line at the Department of Earth and Planetary Sciences at Harvard University. For fluorination, 2–4 mg of Ag_2S was prepared in alumina packets that were placed in a nickel reaction vessel. Samples were reacted at 250 °C overnight (~8 h) with excess fluorine gas to produce SF_6. The SF_6 gas was then purified cryogenically and by gas chromatography prior to analyses on a dual inlet gas source mass spectrometer (Thermo Scientific MAT 25). Two different international standards (IAEA S1, S3) were measured throughout the analytical sessions. The $\delta^{34}S$, $\Delta^{33}S$, and $\Delta^{36}S$ compositions of these standards, recently calibrated by Johnston et al. (2014), were used to anchor our data on a V-CDT scale. For our analyses we assume that IAEA-S-1 is $\delta^{34}S = -0.3‰$, $\Delta^{33}S = 0.107‰$, and $\Delta^{36}S = -0.5‰$ and IAEA-S-3 is $\delta^{34}S = -32.3‰$, $\Delta^{33}S = 0.089‰$, and $\Delta^{36}S = -0.4‰$ versus V-CDT (Ding et al., 2001; Masterson, 2016). From the measurement of these standards, the long-term reproducibility (1σ) of a single fluorination (here including all chemistry and separation) is 0.3‰, 0.008‰, and 0.2‰ for $\delta^{34}S$, $\Delta^{33}S$, and $\Delta^{36}S$, respectively (Johnston et al., 2014). A detailed description of the extraction procedure can be found in Johnston et al. (2007).

3.1.2. Definitions

The sulfur isotope ratios are reported in the conventional delta-notation

$$\delta^x S = \left(\frac{{}^x R_{sample}}{{}^x R_{reference}} - 1 \right) * 1000, \quad (1)$$

with ${}^xR$ being the isotope ratio $^xS/^{32}S$ (x = 33, 34, 36) of the sample and the reference material. Sulfur isotope values are reported relative to the Vienna-Canyon Diablo Troilite

Table 1
Multiple sulfur isotope composition of the studied ultramafic rocks.

Sample name	Location[a]	Fraction	$\delta^{33}S$ (‰)	$\delta^{34}S$ (‰)	$\delta^{36}S$ (‰)	$\Delta^{33}S$ (‰)	$\Delta^{36}S$ (‰)
897C_6	ODP Leg 149	AVS	−11.22	−21.94	−42.51	0.138	−1.225
897C_7	ODP Leg 149	AVS	−10.33	−20.24	−39.26	0.140	−1.156
897C_7	ODP Leg 149	CRS	−5.79	−11.35	−22.05	0.072	−0.584
897D_11	ODP Leg 149	CRS	−8.68	−16.83	−32.34	0.028	−0.600
897D_15	ODP Leg 149	AVS	−10.96	−21.44	−41.55	0.138	−1.201
1070A_1	ODP Leg 173	AVS	−21.91	−42.31	−79.80	0.110	−0.933
1070A_1	ODP Leg 173	CRS	−10.38	−20.01	−37.65	−0.021	0.031
1070A_2	ODP Leg 173	AVS	−22.51	−43.47	−81.89	0.117	−0.921
1070A_2	ODP Leg 173	CRS	−14.91	−28.78	−54.47	0.021	−0.495
1070A_3	ODP Leg 173	AVS	−22.13	−42.72	−80.32	0.103	−0.717
1070A_3	ODP Leg 173	CRS	−9.40	−18.12	−34.29	−0.025	−0.148
1070A_4	ODP Leg 173	AVS	−21.19	−40.93	−77.21	0.100	−0.874
1272A_6	ODP Leg 209	AVS	−18.08	−35.04	−66.30	0.120	−0.776
1272A_6	ODP Leg 209	CRS	−12.98	−25.24	−48.53	0.099	−1.117
1272A_8	ODP Leg 209	AVS	−16.26	−31.54	−59.99	0.112	−0.918
1272A_10	ODP Leg 209	AVS	−14.05	−27.33	−52.30	0.114	−1.025
1272A_10	ODP Leg 209	CRS	−10.72	−20.96	−40.62	0.124	−1.177
1268A_1	ODP Leg 209	AVS	4.33	8.42	15.67	0.004	−0.385
1268A_1	ODP Leg 209	CRS	3.60	6.97	12.94	0.015	−0.343
1268A_2	ODP Leg 209	AVS	2.45	4.70	8.57	0.031	−0.382
1268A_2	ODP Leg 209	CRS	2.13	4.12	7.41	0.013	−0.427
LA3	N. Apennine	CRS	−6.51	−12.48	−23.55	−0.062	0.022
LA12	N. Apennine	AVS	3.73	7.33	13.93	−0.041	−0.035
LA12	N. Apennine	CRS	3.16	6.21	11.70	−0.034	−0.130
LA15	N. Apennine	CRS	−5.12	−9.79	−18.48	−0.062	0.039
LA18	N. Apennine	AVS	−11.21	−21.60	−40.87	−0.026	−0.229
LA18	N. Apennine	CRS	−11.69	−22.49	−42.48	−0.039	−0.187
LA20b	N. Apennine	AVS	−11.80	−22.71	−42.86	−0.036	−0.151
LA20b	N. Apennine	CRS	−11.25	−21.68	−41.05	−0.021	−0.256
LA22_1	N. Apennine	CRS	−2.72	−5.17	−9.70	−0.053	0.101
LMO27	N. Apennine	AVS	0.25	0.55	1.05	−0.037	0.005
LMO27	N. Apennine	AVS	0.36	0.78	1.57	−0.040	0.085
LMO27	N. Apennine	CRS	2.32	4.57	8.71	−0.027	0.015
LMO28	N. Apennine	AVS	−2.46	−4.68	−8.90	−0.052	−0.033
LMO28	N. Apennine	CRS	−1.64	−3.08	−5.68	−0.053	0.155
LMO28_cc	N. Apennine	AVS	−1.44	−2.70	−5.12	−0.048	0.001
LMO28_cc	N. Apennine	CRS	−1.67	−3.15	−5.99	−0.051	−0.015
LSA1	N. Apennine	CRS	−14.43	−27.79	−52.50	−0.016	−0.356
LCM7	N. Apennine	AVS	2.48	4.85	9.15	−0.017	−0.094
LCM7	N. Apennine	CRS	2.81	5.47	10.49	−0.003	0.078
LLB_8	N. Apennine	CRS	7.68	14.92	28.26	0.022	−0.272
SE_P5	Santa Elena	AVS	6.04	11.77	22.29	−0.004	−0.194
SE_P5	Santa Elena	CRS	4.97	9.60	17.98	0.034	−0.346
SE10_01	Santa Elena	AVS	0.54	1.07	1.85	−0.008	−0.172
SE10_12	Santa Elena	AVS	1.15	2.25	4.14	−0.010	−0.149
RC_SP2b	Santa Elena	AVS	9.84	19.12	36.06	0.039	−0.579
SE-SP4b	Santa Elena	AVS	−6.38	−12.46	−24.13	0.051	−0.590
SE-SP4b	Santa Elena	CRS	−7.89	−15.38	−29.78	0.063	−0.764
SE_SP5	Santa Elena	AVS	5.35	10.39	19.57	0.008	−0.266
SE_SP5	Santa Elena	CRS	4.72	9.18	17.30	0.000	−0.221
SE_SP7b	Santa Elena	AVS	11.98	23.21	43.66	0.097	−0.892
SE_SP7b	Santa Elena	CRS	5.88	11.33	20.91	0.062	−0.720
SE-SP10b	Santa Elena	AVS	7.21	14.04	26.49	0.006	−0.355
SE-SP10b	Santa Elena	CRS	3.93	7.64	14.29	0.005	−0.284
SE-SP12	Santa Elena	AVS	4.96	9.67	18.18	−0.005	−0.261
SE-SP14	Santa Elena	AVS	5.73	11.20	21.33	−0.019	−0.061

[a] Original names of ODP samples and coordinates of N. Apennine samples are provided in Supplementary Table S1. Sample location from Santa Elena samples can be found in Schwarzenbach et al. (2016b).

(V-CDT) standard and in parts per thousand (‰). For determination of $\Delta^{33}S$ and $\Delta^{36}S$, we use the following definitions (Farquhar et al., 2000b, 2000c):

$$\Delta^{33}S = \delta^{33}S - 1000\left[\left(1+\frac{\delta^{34}S}{1000}\right)^{0.515} - 1\right] \quad (2)$$

and

$$\Delta^{36}S = \delta^{36}S - 1000\left[\left(1+\frac{\delta^{34}S}{1000}\right)^{1.90} - 1\right]. \quad (3)$$

Due to the low isotopic abundance of ^{36}S, measurement of $\Delta^{36}S$ is not as precise as $\Delta^{33}S$. Given the present error on ^{36}S, $\Delta^{33}S$ and $\Delta^{36}S$ reveal similar information, and although we report both $\Delta^{33}S$ and $\Delta^{36}S$ values, we only discuss the $\Delta^{33}S$ data.

3.1.3. In situ sulfur isotope analyses

Selected samples were chosen for *in situ* analyses of $\delta^{34}S$ of individual pyrite, pyrrhotite and pentlandite grains via Secondary Ionization Mass Spectrometry (SIMS). Analyses were performed on a CAMECA IMS 1280 (monocollector) at the Northeast National Ion Microprobe Facility (NENIMF) at the Woods Hole Oceanographic Institute. Samples for SIMS analyses were selected after detailed microscopic examination on thin sections and bulk rock isotopic analysis. Rock chips were then drilled out using a microdrill, mounted in 1 inch round sections and polished for analyses. The mineralogy of all grains was determined by SEM (scanning electron microscopy) prior to SIMS analyses. Only the isotopic compositions of grains larger than ~30 μm were determined. Where mineral phases were intergrown, grain boundaries were avoided if possible. The presence of intergrowths between different mineral phases below the surface cannot entirely be excluded, however, the analysis pits were examined after the analyses to identify the occurrence of additional sulfur bearing phases.

Measurements on the SIMS were conducted using a Cs^+ primary beam, 10 kV accelerating voltage and 1–2 nA beam current. A raster was applied to the primary beam to achieve a final spot size of 20–25 μm. The mass resolving power was ~4000. A secondary field aperture to block transmission of ions from outside of the innermost ~12.5 μm of the pit was used to reduce the influence of ionization from the sample surface and crater wall. The following sulfide standards were used: Balmat pyrite ($\delta^{34}S = +15.1 \pm 0.2$‰), Rutan pyrite ($\delta^{34}S = +1.2 \pm 0.1$‰), Anderson pyrrhotite ($\delta^{34}S = +1.4 \pm 0.2$‰) (Crowe and Vaughan, 1996), and the in-house standards M8534 pyrrhotite and pentlandite ($\delta^{34}S = +3.6 \pm 0.5$‰), and 40289 pyrrhotite ($\delta^{34}S = +7.0 \pm 0.5$‰). Standards were measured repeatedly to ascertain that the instrumental mass fractionation (α) was statistically constant and to correct for variations in α. The variation of α was accounted for by dividing the standard-derived α by days, and taking an average (and standard deviation) for each day, which was then applied for the standards to the unknowns run on the same day. Reproducibility of the analyses is on average $2\sigma = \pm 1.0$‰, but always $<\pm 2.3$‰ (see supplementary Table S2). The measurement data are shown after correcting for faraday detector background, time interpolation and 2σ data filtering as commonly done for data reduction of isotope data measured on monocollector SIMS.

4. RESULTS

4.1. Bulk rock multiple sulfur isotope compositions

The studied samples preserve significant differences in isotopic composition ($\delta^{34}S$, $\Delta^{33}S$) between locations, and samples from individual locations show distinct relationships between $\delta^{34}S$ and $\Delta^{33}S$ (Fig. 2). The multiple sulfur isotope compositions of the studied samples are summarized in Table 1. Sulfur contents and $\delta^{34}S$ compositions of all the samples are reported in supplementary Table S1 and are within the range of those reported previously (Alt and Shanks, 1998; Alt et al., 2007; Schwarzenbach et al., 2012, 2016b). Hence, not all this data will be discussed here in detail.

In the N. Apennine serpentinites, $\Delta^{33}S_{sulfide}$ values have a relatively narrow range (−0.062 to 0.022‰), are typically negative, and AVS and CRS extracts are not clearly distinguishable. In contrast, a wide range in composition characterizes the $\delta^{34}S_{sulfide}$ with −27.8 to +14.9‰. Both AVS and CRS from the Santa Elena samples have $\delta^{34}S$ that ranges from near 0‰ to distinctly positive values of up to +23.2‰ with AVS typically having more positive values than CRS. $\Delta^{33}S_{sulfide}$ values are between −0.019 and 0.097‰ with no clear distinction between AVS and CRS. At the Iberian Margin ODP Sites 897 and 1070, the $\delta^{34}S_{sulfide}$ is between −44.0‰ and +17.5‰, with very negative $\delta^{34}S$ values (−44.0 to −32.7‰) in the AVS fraction at Site 1070. Similarly, $\Delta^{33}S_{sulfide}$ has a wide range of values, from −0.025‰ to 0.140‰, which overlaps with the range of the total sulfide extracts analyzed in Ono et al. (2012) ($\Delta^{33}S_{sulfide} = 0.001$–$0.161$‰). Overall, AVS at both Sites 897 and 1070 has more positive $\Delta^{33}S$ values (0.100–0.140) than the CRS fraction (−0.025 to 0.072) (Fig. 2). AVS and CRS from the 15°20′N FZ, Site 1272 have negative $\delta^{34}S$ values between −35.4 and −18.9‰, with AVS having more negative values than CRS, and a narrow range in $\Delta^{33}S$ values (0.099–0.124‰). In contrast, at ODP Site 1268 $\delta^{34}S_{sulfide}$ values are positive (3.8–8.6‰) and $\Delta^{33}S_{sulfide}$ values are near zero to slightly positive (0.004–0.031‰). These values are well within the range of those presented in Ono et al. (2012) ($\Delta^{33}S_{sulfide} = 0.007$–$0.038$‰, Fig. 2).

4.2. *In situ* sulfur isotope compositions

The distribution of the *in situ* isotope analyses is shown in Fig. 3. Due to restrictions placed with available sulfur isotope standards for SIMS analyses only the isotopic composition of pyrite, pyrrhotite and pentlandite grains were analyzed. However, these mineral phases represent the majority of the sulfide mineralogy present in the investigated samples, with the exception of those from Santa Elena. These contain a variety of Cu-sulfides (Schwarzenbach et al., 2014), and therefore, no samples from the Santa Elena ophiolite were selected for *in situ* analysis. Given the large range in isotopic composition of

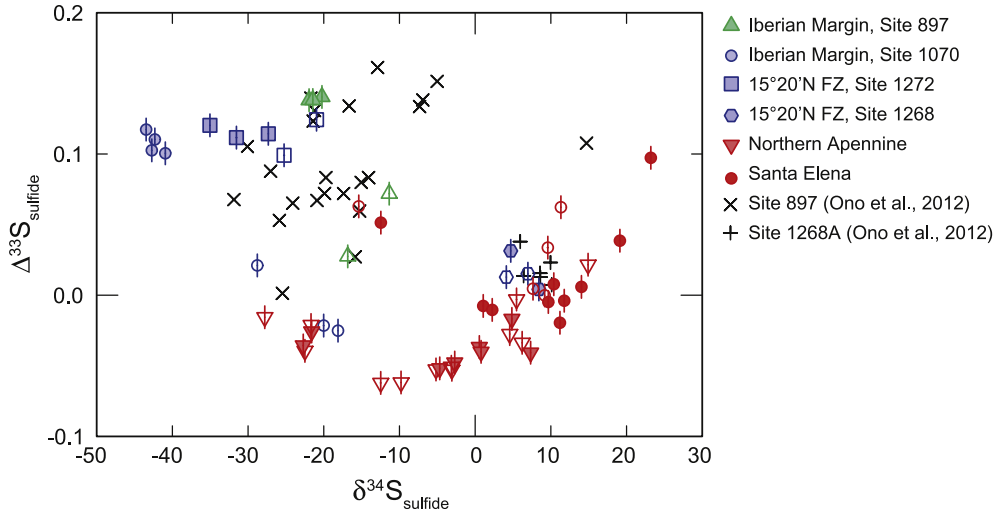

Fig. 2. $\Delta^{33}S$ versus $\delta^{34}S$ of the samples analyzed in this study and samples presented in Ono et al. (2012). The vertical bars show the analytical errors on $\Delta^{33}S$. Errors for $\delta^{34}S$ are smaller than the symbols. Filled symbols are AVS extracts, open symbols are CRS extracts.

the bulk sulfides from the N. Apennine, we focused on the sulfides within these serpentinites in order to investigate this variability. Sulfide grains from the Iberian Margin and the 15°20′N FZ samples were frequently too small for SIMS analyses, thus only a few ODP samples were examined for their *in situ* sulfide $\delta^{34}S$ composition.

4.2.1. Northern Apennine serpentinites

The studied serpentinites from the N. Apennine reveal a large range in *in situ* sulfide $\delta^{34}S$ values (−33.8 to +13.3‰), which is slightly larger than bulk rock analyses (supplementary Tables S1, S2). Overall, pyrite has higher $\delta^{34}S$ (average $\delta^{34}S = 3.5 \pm 6.4$‰) compared to pentlandite and pyrrhotite, whose compositions are negative to slightly positive (average $\delta^{34}S = -10.6 \pm 12.2$‰ and -6.7 ± 8.5‰, respectively) (Fig. 3a). One generation of euhedral pyrite grains that is hosted in the serpentine mesh texture has distinctively positive $\delta^{34}S$ values of +2.0 to +10.2‰ (Fig. 4a–c). In contrast, pyrite hosted in calcite veins has negative $\delta^{34}S$ compositions between −9.7 and −0.3‰. The exception are several grains where pyrite with $\delta^{34}S$ up to +13.3‰ is intergrown with pyrrhotite and pentlandite that have intermediate $\delta^{34}S$ values of −10.8 to +4.1‰ (Fig. 4d and e). These grains also occur within calcite veins (Fig. 4e) or along the edge of calcite veins (Fig. 4d), and overall show a large isotopic variability within single grains (−8.5 to +13.3‰ and −10.2 to +13.1‰). In general, pyrrhotite and pentlandite hosted in calcite veins are characterized by negative $\delta^{34}S$ values (Fig. 4f–h), and where only pyrrhotite and pentlandite are intergrown and filling the entire width of a calcite vein (Fig. 4i) $\delta^{34}S$ values may be as low as −33.8‰.

4.2.2. Iberian Margin

Only one serpentinite from the Iberian Margin was examined by SIMS due to the small grain size of most of the observed sulfide minerals. The studied sample only contains pyrite and shows a narrow range in $\delta^{34}S$ of −13.3 to −9.1‰ (Fig. 3b). All the analyzed pyrite grains are hosted within carbonate-veins.

4.2.3. 15°20′N Fracture Zone

The two studied samples from the 15°20′N FZ, Site 1268 have a range in $\delta^{34}S$ of −12.1 to +14.7‰ with pyrrhotite typically having higher values (average $\delta^{34}S = +5.9 \pm 6.0$‰) than pyrite (average $\delta^{34}S = -4.7 \pm 7.6$‰) (Fig. 3c). Two groups can be distinguished based on their mineralogy and sulfur isotope compositions: Group 1 consists of dominantly pyrite with $\delta^{34}S$ values of −12.1 to −4.7‰ (Fig. 4j and k) and group 2 consists of pyrrhotite with $\delta^{34}S$ values of +6.7 to +14.7‰ (Fig. 4 l and m). Though, one pyrrhotite grain has a composition of −8.4 to +2.3‰. Group 1 sulfides are commonly hosted in carbonate veins, show decomposition features (Fig. 4 k), or grains are locally rounded. Group 2 sulfides are commonly hosted within the serpentine mesh texture.

5. DISCUSSION

Serpentinization of ultramafic oceanic lithosphere is induced by mantle exposure along slow- to ultra-slow spreading mid-ocean ridges and rifted continental margins (Cannat, 1993; Boschi et al., 2006a; Cannat et al., 2006; Dick et al., 2003) with alteration temperatures of <100–500 °C depending on the presence of mafic intrusions (Agrinier and Cannat, 1997; Boschi et al., 2008; Früh-Green et al., 2004, 1996; Schwarzenbach et al., 2013). If mafic intrusions act as heat sources in peridotite-hosted systems, vent fluids are around 350–400 °C, acidic and metal-rich (Charlou et al., 2002; Douville et al., 2002) and thus are chemically similar to basalt-hosted vent fluids that have the potential to produce massive sulfide deposits (e.g., von Damm, 1990; German et al., 2016). In contrast, in the absence of a magmatic heat source serpentinization temperatures are <150–200 °C, the produced fluids are alkaline and Ca-rich and result in calcium carbonate precipitation (Kelley et al., 2001). Additionally, sulfur cycling maybe dominated by sulfate-reducing microorganisms that live at temperatures <∼120 °C (Brazelton et al., 2006; Kelley et al., 2005; Takai et al., 2008). Thus, temperatures strongly

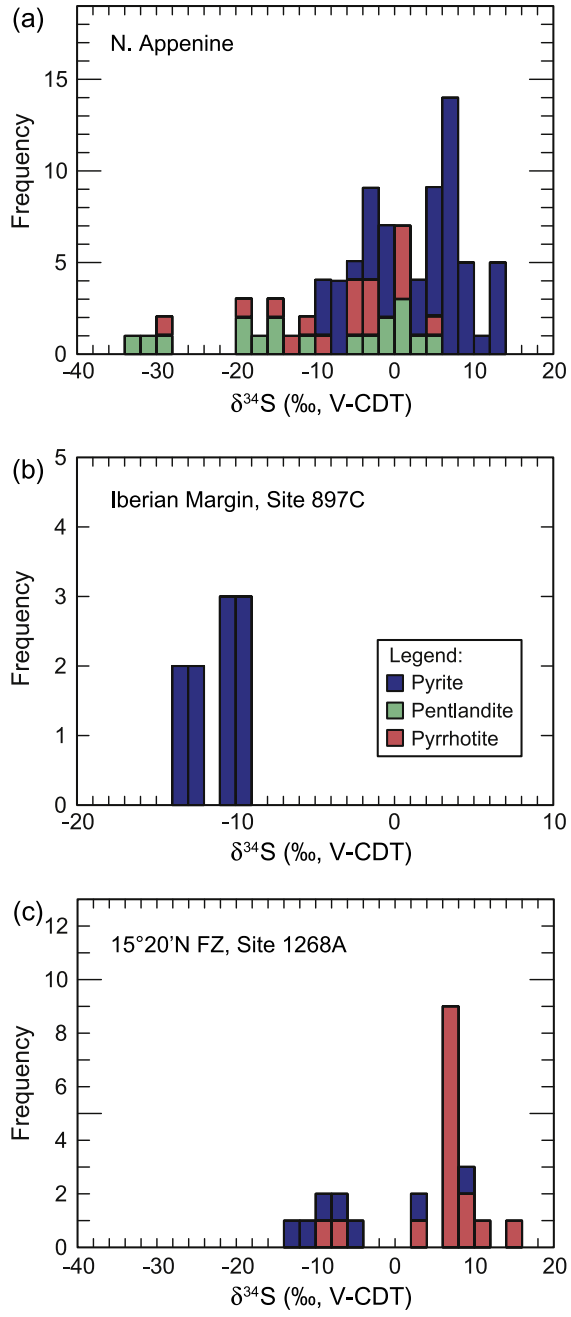

Fig. 3. Histogram of *in situ* $\delta^{34}S$ analyses delineated by mineralogy. (a) N. Apennine: pyrite has dominantly positive $\delta^{34}S$ values, whereas pentlandite and pyrrhotite have dominantly negative $\delta^{34}S$ values to values around 0‰. (b) Iberian Margin: only pyrite was analyzed, which had consistently negative $\delta^{34}S$ values. (c) 15°20′N FZ: serpentinite samples from Hole 1268A comprise pyrrhotite with dominantly positive $\delta^{34}S$ values and pyrite with dominantly negative $\delta^{34}S$ values.

control the extent of abiogenic and biogenic processes and the resulting sulfur geochemistry.

In the following, we model the isotopic compositions that result from mixing different sulfur pools and the activity of several processes that cycle sulfur at different temperatures in peridotite-hosted systems in order to identify the key processes that occurred during the alteration of the studied samples. Models similar to those discussed below have been presented by Ono et al. (2012) who constructed two-component mixing models. We use a similar approach and include both open and closed system behavior (see detailed description in the supplementary material) and consider the impact of two and three-component mixing. Our model results are then discussed in the context of the *in situ* $\delta^{34}S_{sulfide}$ data and mineralogical and petrological observations to constrain the temporal sequence of the processes that took place during water-peridotite interaction in the studied systems.

5.1. General constraints for model calculations

The model calculations presented here consider: (1) the mixing of sulfide (H_2S) from two to three pools with distinct sulfur isotope compositions. For example, mantle sulfide [$\delta^{34}S_{mantle} \approx 0 \pm 1$‰ (Sakai et al., 1984; Shanks et al., 1995)] or sulfide produced through a specific mechanism involving isotopic fractionation (e.g., reduction of SO_4^{2-} to H_2S). Thus, sulfate (SO_4) is only included as initial component that is converted to H_2S through abiogenic and/or biogenic processes. And (2) we assume that the isotopic composition of the analyzed sulfide minerals closely corresponds to the isotopic composition of the H_2S in the fluid; Fractionation factors between H_2S and pyrite at T = 200–350 °C result in $\Delta_{pyrite\text{-}H2S} = 1.8$–$1.0$‰, and increase to 2.2‰ at 150 °C (Ohmoto and Rye, 1979). The $\Delta_{pyrite\text{-}H2S}$ may be as high as −1.9‰ in hydrothermal vents (Syverson et al., 2015). Since these fractionations are considerably smaller than the range of values measured in the studied systems, neglecting isotope fractionation between fluid and mineral does not meaningfully affect our interpretation of the data.

5.1.1. Calculation of mixing and fractionation effects

In the two-component mixing models we use the common mass balance equation:

$$\delta^X S = f * \delta^X S_A + (1 - f) * \delta^X S_B \quad (4)$$

where x = 33,34, A and B represent the two sulfide pools that are mixed, and f = fraction of pool A. We assume that the ratios of $^{34}S/^{32}S$ and $^{33}S/^{32}S$ follow mass dependent fractionations with θ exclusively dependent on temperature (see definition below), which may not always be the case, especially for biogenic processes (e.g., Johnston et al., 2007). However, due to the complexity of biogenic and abiogenic processes involved in peridotite-hosted systems the model calculations below provide a useful approximation to reconstruct the effects of different processes on the sulfur geochemistry of the serpentinites. In order to model SO_4-H_2S fractionation for $^{34}S/^{32}S$ and $^{33}S/^{32}S$ ratios we relate $^{33}\alpha$ and $^{34}\alpha$ with the factor θ in the mass-dependent fractionation relationship (after Farquhar et al., 2003 and references therein):

$$\theta = \frac{\ln(^{33}\alpha)}{\ln(^{34}\alpha)} \quad (5)$$

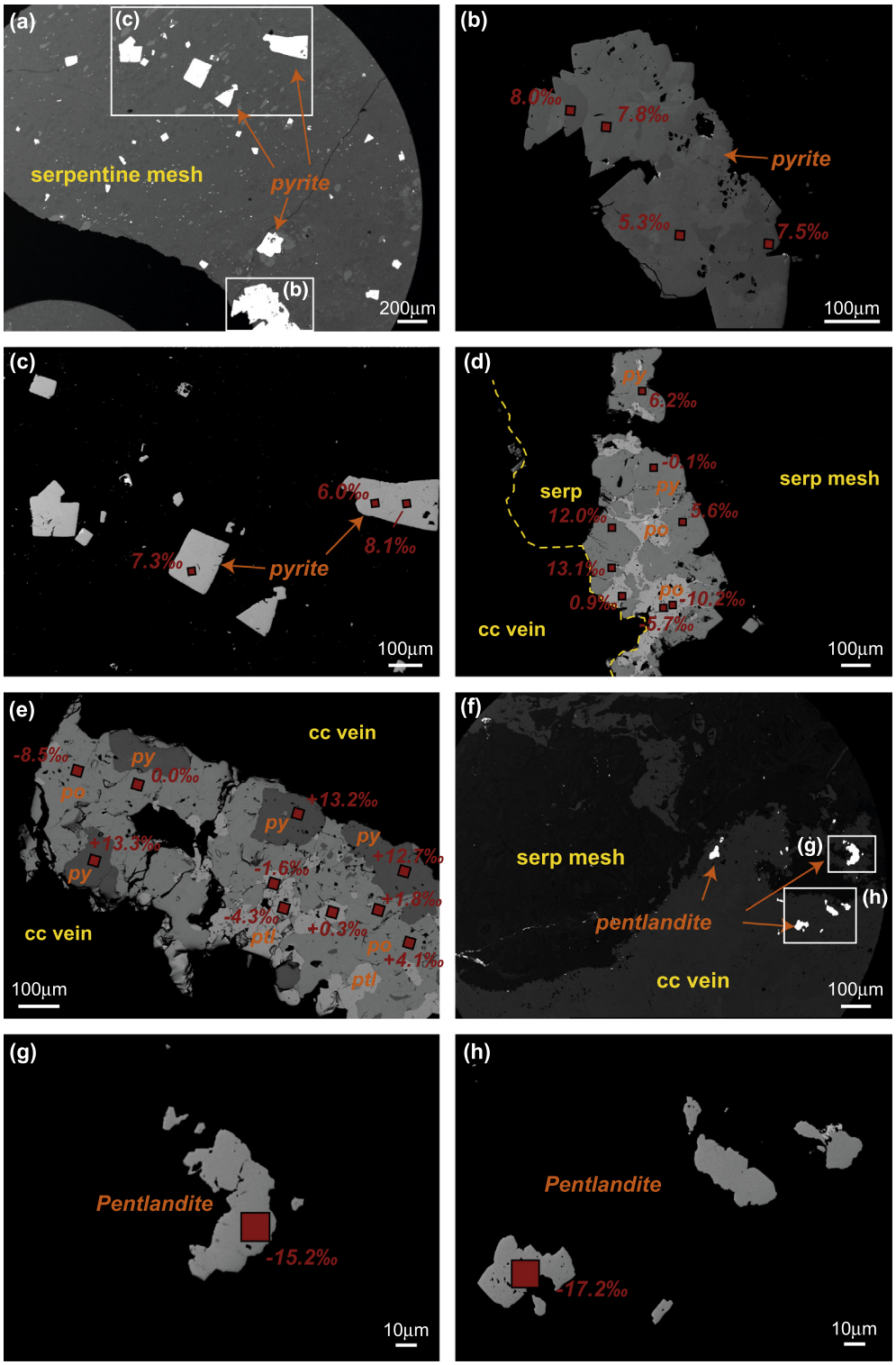

Fig. 4. BSE images and $\delta^{34}S$ compositions of sulfide grains from the N. Apennine serpentinites (a–i) and the 15°20′N FZ (j–m) analyzed by SIMS. (a) Euhedral pyrite grains in the serpentine mesh-texture; (b) and (c) Pyrite grains having positive $\delta^{34}S$ values. (d) and (e) Multi-phase sulfide grains in a calcite vein with pyrite having positive $\delta^{34}S$ values up to +13.3‰ intergrown with pyrrhotite and pentlandite having lower $\delta^{34}S$ values than pyrite. Distinct replacement features are evident with pyrite being replaced by pentlandite and/or pyrrhotite. (f) Pentlandite grains within calcite veins; (g) and (h) pentlandite with negative $\delta^{34}S$ values. (i) Sulfide grain of intergrown pyrrhotite and pentlandite showing strong isotopic heterogeneities. Here the sulfide is filling the whole width of a calcite vein. (f) and (g): Sulfides in calcite veins from the 15°20′N FZ show two groups of sulfide compositions (though overlapping): (j and k) one consists of pyrite with negative $\delta^{34}S$ values that show extensive decomposition features (such as irregular grain boundaries) and are hosted within a carbonate vein network, and (l and m) one group of pyrrhotite grains with positive $\delta^{34}S$ values that are hosted within the serpentine mesh texture. Abbreviations: cc = calcite, serp = serpentine, carb = carbonate.

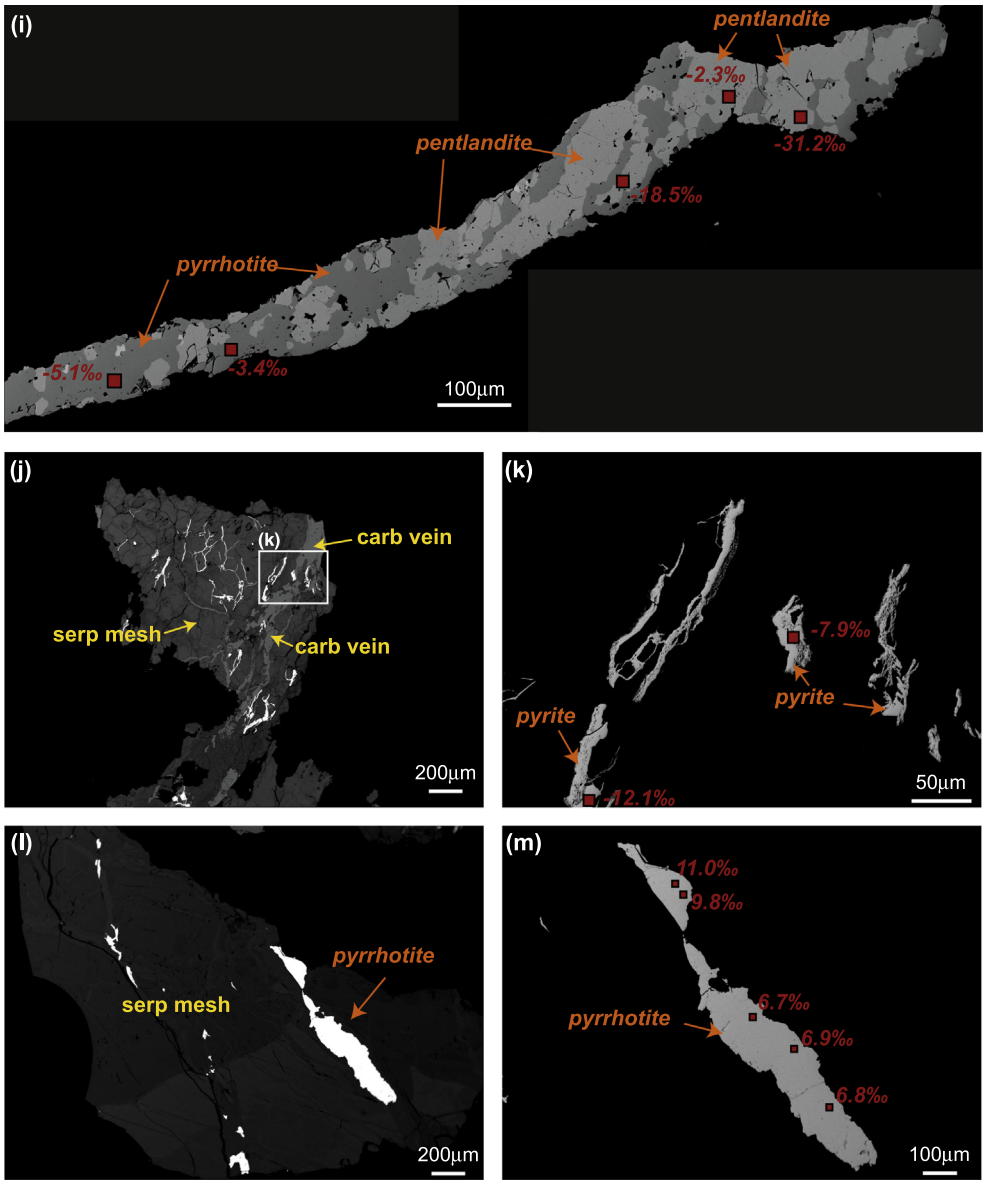

Fig 4. *(continued)*

For equilibrium mass-dependent fractionation, θ ranges between 0.514 and 0.516 (Farquhar et al., 2003). For temperatures typical for serpentinization environments (150–500 °C) θ approaches 0.5154 and can be calculated from the empirical equation [Eq. (6)]:

$$\theta_{eq} = -9.460 * T^{-2} - 0.3117 * T^{-1} + 0.5159, \quad (6)$$

where T is temperature in Kelvin (Ono et al., 2007). For microbial processes, θ values can have a larger range because biogenic processes typically involve multiple fractionation steps and incomplete transfer of sulfur-bearing species. This results in $\Delta^{33}S$ values that are ≠ 0. Specifically, θ values of 0.509–0.519 have been measured for biogenic processes, with sulfate reduction generating values less than 0.515 (Johnston et al., 2005; Ono et al., 2012).

5.1.2. Determination of input values: mantle sulfur and seawater sulfate

The main sources of sulfur in peridotite-hosted hydrothermal systems are mantle sulfur (predominantly sulfide) and seawater-derived sulfate (SO_4). We define mantle sulfur as sulfide in the unaltered peridotite, which is typically present as pentlandite ± pyrrhotite ± chalcopyrite (Lorand, 1989a, 1989b). The isotopic composition of the primary mantle sulfide is estimated to be around $\delta^{34}S \approx 0 \pm 1‰$ (Sakai et al., 1984; Shanks et al., 1995), with recent estimates for MORB of $\delta^{34}S = -0.91 \pm 0.50‰$ (Labidi et al., 2012). The $\Delta^{33}S$ of the mantle is estimated to have a near-zero value (Labidi et al., 2012; Ono et al., 2012, 2007). For the model calculations we use $\delta^{34}S_{mantle} = 0.0‰$ and $\Delta^{33}S_{mantle} = 0.000‰$ in line with these previous

studies, however, deviations from this value are considered below. Sulfur concentrations of the fertile mantle are ~250 ppm (Lorand, 1991) and 60–120 ppm in depleted mantle (Salters and Stracke, 2004; Alt et al., 2007). Unless otherwise noted, we assume a depleted mantle composition of 120 ppm S, which is typical for mid-ocean ridge settings. Though, we note that changes in mantle sulfur content only modify the model calculations slightly (see discussion below).

Modern seawater sulfate has a $\delta^{34}S_{sulfate}$ value of $+21.15 \pm 0.15‰$ and $\Delta^{33}S_{sulfate}$ of $0.048 \pm 0.006‰$ (Johnston et al., 2014). However, most of the studied locations represent ancient oceanic lithosphere serpentinized in the Mesozoic (Santa Elena ophiolite: ~130–120 Ma (Madrigal et al., 2015), Iberian Margin: ~120–110 Ma (Whitmarsh and Wallace, 2001); Northern Apennine: ~160–140 Ma (Lagabrielle and Cannat, 1990)), where marine SO_4 isotope compositions and concentrations deviated from modern seawater. In the Jurassic and Cretaceous SO_4 concentrations were overall lower (2–12 mM) with a $\delta^{34}S_{sulfate}$ range between 14 and 22‰ (Horita et al., 2002; Kampschulte and Strauss, 2004; Paytan et al., 2004; Timofeeff et al., 2006; Wortmann and Paytan, 2012). For our models, we use an intermediate Mesozoic SO_4 concentration of 10 mM, $\delta^{34}S_{sulfate} = 18‰$ and a $\Delta^{33}S_{sulfate}$ value of $0.043 \pm 0.016‰$ for Cretaceous seawater-sulfate as determined by Masterson et al. (2016). The modern seawater sulfate composition is used in some model calculations for comparison with the samples recovered near the 15°20′N FZ, which were serpentinized in the Cenozoic (see also supplementary Figs. S1, S2).

5.2. End-member mixing models for peridotite-hosted systems

5.2.1. High temperature systems

Sulfur cycling in high temperature systems is mostly controlled by anhydrite precipitation, thermochemical sulfate reduction (TSR), and leaching of magmatic sulfides (e.g., Ohmoto and Lasaga, 1982; Shanks, 2001; Ono et al., 2007). In typical basalt-hosted systems, precipitation of anhydrite at >150 °C removes the majority of seawater-derived SO_4 from the fluid – >90% of the SO_4 is removed leaving ~0.2–3.3 mM SO_4 – but is dependent on the availability of Ca^{2+} (Seyfried and Bischoff, 1981; Shanks, 2001). Further heating to >250 °C converts the remaining SO_4 to H_2S via TSR and magmatic H_2S is incorporated into the fluid (Shanks et al., 1981). Similarly, in peridotite-hosted systems fluids are heated and modified at depth in the vicinity of gabbroic intrusions or mafic dikes, before they interact with the peridotite that is undergoing serpentinization (Alt and Shanks, 2003). Evidence suggests these processes were active during alteration at ODP Site 1268 (Alt et al., 2007) and in the Santa Elena peridotites (Schwarzenbach et al., 2014, 2016b). In the following, we model the effects of both open (model 1) and closed system TSR (models 2 and 3), and the mixing of this sulfide with basaltic-derived sulfide (model 4).

Model 1 (Fig. 5a) shows effects of two-component mixing between mantle sulfur and hydrothermal sulfide produced by open system thermochemical reduction of seawater-derived SO_4. Using the equation from Ohmoto and Lasaga (1982) [Eq. (7)] an enrichment factor of 29–11‰ is calculated (for T = 200–500 °C) for SO_4-H_2S fractionation during TSR:

$$\varepsilon_{SO4-H2S} = \left[\frac{6.463 * 10^6}{T^2} + 0.56\right] \quad (7)$$

For hydrothermal fluids of ~350–400 °C this results in $\delta^{34}S_{sulfide}$ values of around + 3 to +6‰. Negative $\delta^{34}S_{sulfide}$ values are only possible if temperatures are < 300 °C ($\delta^{34}S_{sulfide}$ as low as −3‰ at 250 °C – below 250 °C TSR is sluggish (Shanks et al., 1981)) or if the initial $\delta^{34}S_{sulfate}$ is <+15‰, which produces $\delta^{34}S_{sulfide}$ values of around −5‰ (at 300 °C). Given these considerations, we interpret negative $\delta^{34}S_{sulfide}$ values as the result of microbial processes rather than abiogenic processes (see discussion below). The θ is calculated as a function of temperature using Eq. (6). Fig. 5a shows the expected isotopic signatures produced at 300–550 °C. With increasing temperature, $\delta^{34}S_{sulfide}$ becomes more positive whereas the model suggests a slight decrease in $\Delta^{33}S_{sulfide}$. However, the change in $\Delta^{33}S_{sulfide}$ strongly depends on the initial $\Delta^{33}S_{mantle}$ composition (see suppl. Fig. S4).

Model 2 (Fig. 5b and c) describes the isotopic evolution of the fluid during closed system TSR using a Rayleigh fractionation model. This process has been suggested for Santa Elena based on bulk rock $\delta^{34}S$ from sulfide and sulfate extracts (Schwarzenbach et al., 2016b). We use the same seawater SO_4 isotope compositions as in model 1, initial mantle sulfur contents of 120 ppm (Fig. 5b) and 250 ppm (Fig. 5c), and a limited reservoir of initial seawater SO_4 assuming anhydrite precipitation: to account for the range of SO_4 concentrations in modern and ancient seawater we use a broad range of SO_4 concentrations between 10 ppm (<0.2 mM) and 2000 ppm (20 mM). The model results displayed in Fig. 5b and c reflect closed system fluid evolution as $\delta^{34}S_{sulfide}$ and $\Delta^{33}S_{sulfide}$ values approach initial seawater SO_4 compositions at temperatures of 350 °C. The initial mantle sulfur and SO_4 isotope compositions thereby control the final isotope composition of the produced H_2S and the initial sulfate $\delta^{34}S$ and $\Delta^{33}S$ controlling the overall trajectory observed in the product H_2S.

Both models 1 and 2 fail to explain $\Delta^{33}S$ values above ~0.04‰. Such values can only be reached with a fluid with an evolved isotopic composition: Model 3 assumes that 60% of the SO_4 was reduced to H_2S by TSR in closed system and was removed from the fluid. This scenario of closed system behavior under low water-rock ratios is in line with previous models for the alteration of the Santa Elena peridotites (Schwarzenbach et al., 2016b). The remaining sulfur in the fluid was then used as the initial composition for model 3. Fig. 5d demonstrates that a highly evolved fluid can account for both very positive $\delta^{34}S_{sulfide}$ and $\Delta^{33}S_{sulfide}$. However, using the assumption stated above at least 3 mM SO_4 would have to be present in the fluid.

Model 4 represents three component mixing that considers the input of basaltic sulfide: (1) 120 ppm of mantle sulfide; (2) H_2S formed by TSR of seawater SO_4 (assuming a

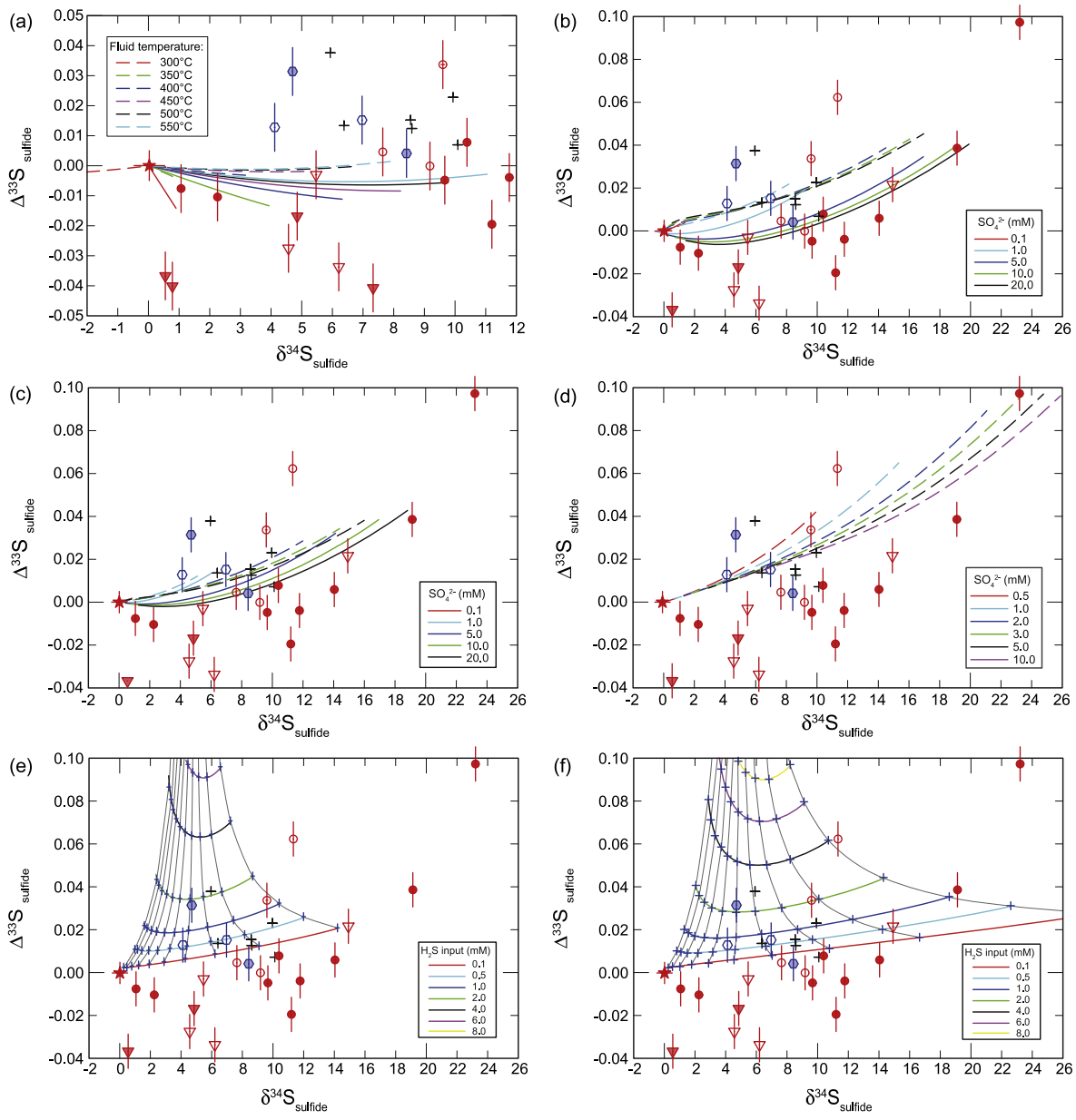

Fig. 5. Model calculations simulating the effects of abiogenic, high temperature processes on the $\delta^{34}S_{sulfide}$ and $\Delta^{33}S_{sulfide}$ composition including the measured data shown for comparison (symbols as in Fig. 2). (a) ***Model 1:*** mixing of mantle sulfide with H_2S derived from TSR in an open system showing the effects at variable fluid temperatures. (b and c) ***Model 2:*** mixing of mantle sulfide with H_2S produced by TSR in a closed system assuming a Rayleigh fractionation model with variable SO_4 concentrations, T = 350 °C, and initial mantle sulfur concentrations of (b) 120 ppm (depleted mantle) and (c) 250 ppm (average mantle). (d) ***Model 3*** assuming interaction with an evolved fluid that underwent loss of 60% SO_4 by TSR in a closed system prior to further fluid-rock interaction ($\delta^{34}S_{sulfate}$ = 33.8‰, $\Delta^{33}S_{sulfate}$ = 0.143‰). The model is calculated for variable SO_4 concentrations. (e and f) ***Model 4*** showing the effects of addition of H_2S that equilibrated in a high-temperature, basalt-hosted system. The model includes variable input of H_2S from black smoker type fluids with $\delta^{34}S$ = 4.95‰ and $\Delta^{33}S$ = 0.028‰, mantle sulfide contents of 120 ppm, T = 350 °C, and SO_4 contents of (e) 1 mM and (f) 2 mM. Dashed lines in a, b, c = models using Mesozoic seawater compositions, solid lines = modern seawater composition also allowing for evaluating the effects of variable sulfate isotope composition.

Mesozoic isotopic composition) in a closed system with 1 mM (Fig. 5e) and 2 mM (Fig. 5f) initial SO_4 (SO_4 contents after anhydrite precipitation); and 3) variable amounts of H_2S sourced from equilibration near a mafic intrusion, such as in fluids venting from the East Pacific Rise (EPR): Ono et al. (2007) reports $\delta^{34}S$ of vent fluid H_2S at the EPR at 9–10°N of +4.43 to +5.85‰ (average + 4.95‰) and $\Delta^{33}S$ values of 0.011–0.048‰ (average 0.028‰). They suggest that these fluids form by mixing of 73–89% of sulfide derived from leaching of magmatic sulfide and 11–27% from the reduction of seawater SO_4 (i.e., TSR) and are typical for high-temperature vent fields (Ono et al., 2007). We

suggest that such a hydrothermal fluid is the most likely source of a component characterized by positive $\Delta^{33}S$ values used in our model calculations (Fig. 5e and f).

5.2.2. Microbial activity in low temperature systems

Low temperature serpentinization systems can host sulfate-reducing microbes that utilize H_2 produced from the serpentinization reaction as an energy source (Brazelton et al., 2006; Lang et al., 2012). Microbial sulfate reduction (MSR) is characterized by large isotope fractionations (Rees, 1973) that can be reflected in the isotopic composition of sulfide minerals in sediments and altered oceanic lithosphere; these sulfides can have very negative $\delta^{34}S$ values, as low as −45‰ e. g., at the Iberian Margin (Alt and Shanks, 1998; Schwarzenbach et al., 2012), but both positive and negative $\Delta^{33}S$ values (Ono et al., 2012, 2006).

In model 5, we mix sulfide produced by MSR in an open system with mantle sulfide (Fig. 6a). For the initial SO_4 compositions we use the values discussed above for Mesozoic seawater. As a maximum isotope fractionation factor between SO_4 and H_2S we assume $\varepsilon = 66‰$ as suggested by Sim et al. (2011), which results in a MSR H_2S end member with $\delta^{34}S_{sulfide} \approx -45$ to −48‰. This agrees with the lowest $\delta^{34}S_{sulfide}$ values measured at the Iberian Margin (supplementary Table S1). Fig. 6a shows the results of model 5 using variable θ values between 0.509 and 0.515 as suggested for biogenic processes and sulfate reducing microbes in particular (Farquhar et al., 2003; Johnston et al., 2005; Ono et al., 2012). This open system model demonstrates that only a few samples can be explained with this simple two-component mixing, even if the θ value is allowed to vary. However, in ultramafic-hosted systems MSR rarely takes place under open system conditions since fluid pathways restrict direct access to the marine SO_4 pool limiting local SO_4 availability. We therefore modeled scenarios with closed system MSR with (1) variable θ values (Fig. 6b) and (2) variable ε values at a fixed $\theta = 0.515$ (Fig. 6c) with an initial Mesozoic seawater sulfate composition.

Overall, these model results suggest that MSR was a dominant process both at the Iberian Margin and the 15° 20′N FZ Site 1272 and in one sample from Santa Elena, assuming variations in SO_4-H_2S fractionation. Ono et al. (2012) performed additional calculations (modeling MSR as a function of temperature) that suggest the unusually low $\delta^{34}S_{sulfide}$ signatures observed at the Iberian Margin are the result of closed system MSR at 2–40 °C. The model calculations performed here also allow reconstruction of the observed data assuming fractionation factors of up to 75‰ with only 10 ppm of the primary mantle sulfide component remaining in the rock, i.e., that the primary sulfide in the rock was almost entirely replaced by secondary sulfide produced by MSR (see supplementary Fig. S2).

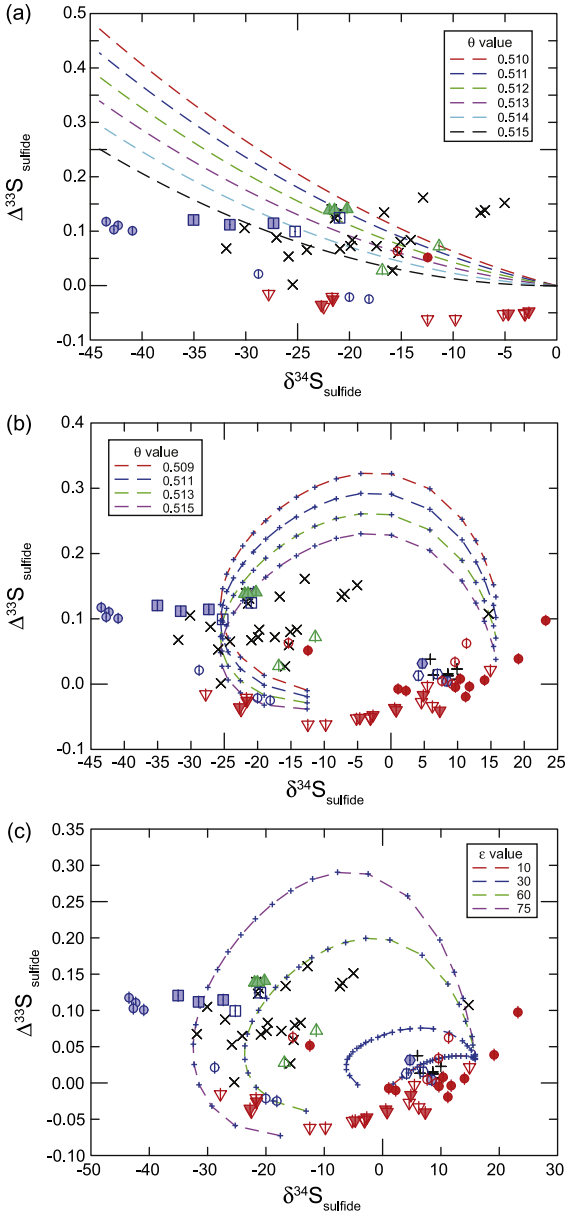

Fig. 6. Model calculations for biogenic processes during fluid-peridotite interaction (symbols as in Fig. 2). All models assuming Mesozoic seawater compositions ($SO_4 = 10$ mM, $\delta^{34}S_{sulfate} = +18‰$, $\Delta^{33}S_{sulfate} = 0.043‰$; mantle: 120 ppm S, $\delta^{34}S_{sulfide} = 0‰$, $\Delta^{33}S_{sulfide} = 0‰$). For modern seawater compositions see supplementary Fig. S1. (a) ***Model 5*** showing the trend expected for simple two component mixing of mantle sulfide with biogenically produced H_2S in an open system, assuming $\varepsilon = 66‰$ and variable θ-values. (b and c) ***Model 6***: Closed system MSR assuming for (b) $\varepsilon = 66‰$ and variable θ-values, and for (c) variable ε values and $\theta = 0.515$.

5.2.3. Effects of sulfide oxidation

The oxidation of sulfide minerals is a common process during extensive water-rock interaction under oxidizing conditions. In the N. Apennine serpentinites oxidation of sulfides is manifested in the pseudomorphic replacement of pyrite crystals by hematite (Schwarzenbach et al., 2012). At the Atlantis Massif, kinetic fractionation during oxidation has been suggested to produce $\delta^{34}S_{sulfide}$ values of up to +15‰ (Delacour et al., 2008b). Fry et al. (1988) experimentally constrained the sulfur isotope fractionation during sulfide oxidation of $-5.2 \pm 1.4‰$ at pH 8–11. Oxidation of sulfide minerals to SO_4 thus would result in progressively

heavier residual sulfide, though, the isotopic effect is only significant (>5%) if more than 40% of the sulfide is oxidized (see supplementary Fig. S3). However, in most cases oxidation only takes place along the grain boundaries and thus the isotopic effects of oxidation are typically minor (Alt et al., 2007). Hence, this process is not modeled here.

5.3. Implications on the evolution of the Santa Elena peridotites

The isotope signatures of the Santa Elena peridotites preserve strong indications of high-temperature processes and some locally retain almost primary mantle isotopic compositions; they have a narrow, near-zero range in $\Delta^{33}S_{sulfide}$ of −0.008 to −0.010‰ (Fig. 2). However, most samples show positive $\delta^{34}S_{sulfide}$ (up to +35.0‰) and $\Delta^{33}S_{sulfide}$ values (up to 0.097‰). These $\delta^{34}S$ signatures have previously been associated with closed system TSR (Schwarzenbach et al., 2016b). Interestingly, closed system TSR alone does not reproduce the observed $\Delta^{33}S$ and $\delta^{34}S$ sulfide values (Fig. 5b and c). Even if a fluid with an evolved isotopic composition caused the highly positive $\delta^{34}S_{sulfide}$ and $\Delta^{33}S_{sulfide}$ values, this process would have required at least 3 mM of SO_4 to remain in the fluid after anhydrite precipitation (Fig. 5d). Alternatively, positive $\Delta^{33}S_{sulfide}$ may also be the result of interaction with a high-temperature fluid that equilibrated in the vicinity of gabbroic intrusions (model 4, Fig. 5e and f). This process is also usually accompanied by TSR. However, even in this case a fluid with at least 2 mM SO_4 was necessary. Interestingly, serpentinization of the Santa Elena ophiolite occurred in the early Cretaceous where multiple lines of evidence suggest that SO_4 concentrations were lower than modern seawater (e.g., Hardie, 1996; Horita et al., 2002; Timofeeff et al., 2006) and, specifically, that Ca/SO_4 ratios of seawater were higher than today (Hardie, 1996). Thus, anhydrite precipitation would cause a higher fraction of SO_4 removal from the initial seawater-derived fluid. One possible explanation for excess SO_4 in the fluid would be that Ca^{2+} concentrations in the serpentinizing fluids were too low to allow for significant sulfate removal by anhydrite formation before TSR occurred. This may be due to calcium carbonate precipitation during fluid influx and recharge (Lang et al., 2012; Proskurowski et al., 2008) or due to restricted availability of Ca in the peridotite (~3.5 wt.% CaO in peridotites (Salters and Stracke, 2004) versus ~9–14 wt.% CaO in gabbros (Casey et al., 2007)) that could result in limited Ca^{2+} supply to the fluid during water-rock interaction compared to mafic-hosted systems (Bach and Humphris, 1999).

Overall, integrating the mineralogical and geochemical data implies that in the Santa Elena peridotites serpentinization took place at <250 °C with local input of higher temperature fluids (>350 °C) that experienced limited SO_4 removal prior to TSR (Schwarzenbach et al., 2014; this study). TSR took place during restricted fluid input, i.e., following closed system fractionation, but also in conjunction with the input of sulfide from gabbroic intrusions. Restricted fluid input is supported by the absence of extensive carbonate veining, generally low degrees of serpentinization, and highly reducing conditions during fluid-rock interaction, as documented by the abundance of Fe-Ni alloys (Schwarzenbach et al., 2014). Closed system evolution also caused the fractionation between the highly reducing phases and less reduced phases; i.e., the AVS fraction evolved at more reducing conditions to produce more positive sulfide isotope compositions than the CRS fraction. These high temperature fluids also resulted in the formation of Cu-bearing sulfides and metals, and caused restricted replacement of pyroxene (Schwarzenbach et al., 2014). However, locally fluid input was limited and the peridotites retain an almost mantle-like isotope signature.

Despite the possibility that some of these rocks may be affected by continental interaction with meteoric fluids, we found no evidence that processes like oxidation of sulfide minerals occurred in the Santa Elena samples. Oxidation would have generated sulfate with a lower isotopic composition compared to the sulfide fraction. However, in almost all the studied samples the sulfate fraction has a higher isotopic composition inferring closed system TSR. One sample provides evidence for MSR as indicated by $\delta^{34}S_{sulfide}$ values of −15.5 to −12.5‰. Whether this took place during serpentinization in an oceanic setting or during continental water-rock interaction cannot be constrained with the available data set.

5.4. Hydrothermal history of the Northern Apennine serpentinites

5.4.1. Imprint of a multi-stage history

The sulfur geochemistry of the N. Apennine serpentinites strongly suggests multiple episodes of sulfur cycling with the processes of MSR, sulfide removal via oxidation and the local input of hydrothermal sulfide all affecting the isotopic composition of these rocks (Schwarzenbach et al., 2012). In contrast to the samples from Santa Elena, the Iberian Margin and the 15°20′N FZ, the serpentinites from the N. Apennine lie on a distinct and curved arc that suggests mixing between a ^{34}S-enriched end member with $\delta^{34}S_{sulfide}$ up to +16.1‰ and a ^{32}S-enriched end member with $\delta^{34}S_{sulfide}$ as low as −33.7‰ (Fig. 2). The large range in isotopic compositions is found in both the bulk rock and the *in situ* isotope data. However, the framework provided by the models presented above cannot explain the data from the N. Apennine. Considering the complex history of these rocks, we created three-component-mixing models to better understand the resulting isotopic compositions (see suppl. Fig. S5). Fig. 7 shows the best fit model and includes: (1) Closed system MSR following a Rayleigh distillation trend assuming an enrichment factor of 66‰, which corresponds to the highest values observed in these systems (see suppl. Table S1), and 10 mM initial seawater SO_4; (2) mixing with 10 ppm mantle sulfide, assuming that water-rock interaction leached almost the entire primary mantle sulfide from the rocks; and (3) introduction of a strongly ^{34}S-enriched high-temperature fluid. As high-temperature fluid composition we used the composition of the most ^{34}S-enriched sample ($\delta^{34}S_{sulfide} = +14.9‰$, $\Delta^{33}S_{sulfide} = 0.022‰$) as an end member that formed through closed system TSR and possibly

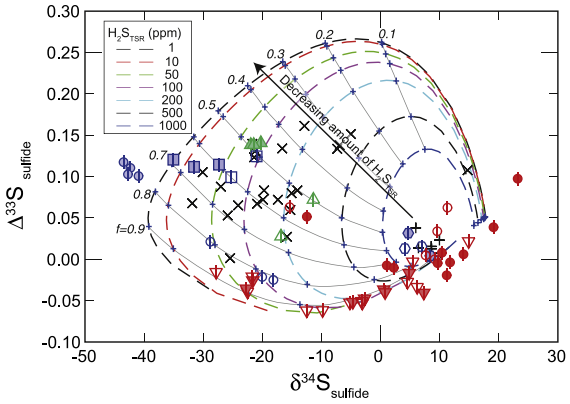

Fig. 7. Model showing the effect of fluid mixing between H_2S derived from MSR produced in a closed system, mantle sulfide (60 ppm S) and variable amounts of H_2S with a ^{34}S-enriched composition ($\delta^{34}S = 14.9‰$, $\Delta^{33}S = 0.022‰$) for example produced by closed system TSR as shown in Fig. 5b. Initial seawater SO_4 corresponds to Mesozoic seawater compositions. The fractions (in italic, e.g., f = 0.9) represent the fractions in the Rayleigh distillation model, with f = 0.9 representing 10% conversion of SO_4 to H_2S by closed system MSR. Symbols as in Fig. 2.

mixing with basaltic-derived H_2S (see Fig. 5). The calculations are shown with variable input of ^{34}S-enriched H_2S from the high temperature fluid. Due to the large number of variables that influence the bulk rock chemistry several models were constructed (see supplementary Fig. S5). The measured data could also be explained assuming, either that the mantle end member has a negative $\Delta^{33}S_{sulfide}$ value, which would allow lower initial SO_4 concentrations (2 mM) in the fluid, or if a higher enrichment factor for Rayleigh distillation (>70‰) is assumed, which, however, has not been observed in these systems.

This model scenario implies that the sulfide geochemistry in the N. Apennine serpentinites was affected by both MSR, as well as, closed system TSR, which produces the observed trend in $\delta^{34}S_{sulfide}$ and $\Delta^{33}S_{sulfide}$ values. The generation of a ^{34}S-enriched fluid by TSR is demonstrated in Fig. 5b. However, we note here that the interaction with gabbro-derived fluids (e.g., H_2S produced by leaching of mafic rocks) cannot entirely be excluded, though they do not reach as positive $\delta^{34}S_{sulfide}$ values as can be produced by closed system TSR. In addition, the model calculations also imply that most of the mantle sulfide was removed from the rock and replaced by secondary sulfides, which is justified considering the extensive degree of water-rock interaction these rocks have experienced (Schwarzenbach, 2011).

5.4.2. Constraints on oxygen fugacities and H_2S activities

In peridotite-hosted hydrothermal systems, the sulfide and metal mineralogy reflects the oxygen fugacity and H_2S activity present during fluid circulation (Frost, 1985). Serpentinization results in highly reducing conditions imposed by the formation of H_2 from the oxidation of ferrous iron in olivine to ferric iron (Bach et al., 2006). While initial olivine hydration allows the stability of native metals and metal alloys (Frost, 1985) extensive fracturing during progressive serpentinization allows for increases in the oxygen fugacity (and decreasing H_2 fugacities). Elevated f_{O2} and H_2S activities are commonly observed during late stages of serpentinization and produce oxidized and sulfur-rich mineral assemblages such as pyrite and vaesite (Alt and Shanks, 1998; Delacour et al., 2008b; Klein and Bach, 2009; Schwarzenbach et al., 2012). The N. Apennine serpentinites are dominated by pyrrhotite, pyrite, pentlandite, millerite, and siegenite (Schwarzenbach et al., 2012). Interestingly, all $\delta^{34}S_{sulfide}$ values above + 4‰ were measured within pyrite, while most negative $\delta^{34}S_{sulfide}$ values were measured in pyrrhotite and pentlandite (Figs. 3 and 4). Assuming that progressive serpentinization of peridotite favors increasingly oxidizing conditions, one would expect to initially find pyrrhotite followed by pyrite. However, petrographic observations imply that early-formed pyrite was locally replaced by pyrrhotite and pentlandite (Fig. 4c and d).

Considering pyrite-pyrrhotite equilibria, at high temperatures higher H_2S activities are required for pyrite to be stable as compared to low temperatures (Klein and Bach, 2009; Schwarzenbach et al., 2014). This implies that during TSR H_2S activities were comparatively higher and the product sulfide formed pyrite. Later, at lower temperatures, less S-rich and/or more reducing conditions facilitated MSR and enabled pyrrhotite formation and the partial replacement of first generation pyrite. Partial mineral dissolution and re-precipitation also explains the intermediate $\delta^{34}S$ values observed in the N. Apennine sulfides (Fig. 4g and h), which would result from mixing of ^{34}S-enriched H_2S from pyrite dissolution with ^{32}S-enriched H_2S formed by MSR. This mechanism also explains the lack of correlation between $\delta^{34}S$ values with mineralogy: AVS (e.g., pyrrhotite) or CRS (e.g., pyrite).

5.4.3. Constraints for the hydrothermal evolution

Considering bulk rock multiple and mineral specific *in situ* sulfur isotope analyses we infer that in the N. Apennine, euhedral pyrite formed initially from a high-temperature fluid (Fig. 8a, area 1). TSR occurred under closed system conditions to produce $\delta^{34}S_{sulfide}$ values up to +16.1‰ with possible input of mafic-derived sulfide. Detachment fault surfaces typically associated with mantle exposure along modern ultra-slow to slow-spreading mid-ocean ridges (Boschi et al., 2006a; McCaig et al., 2007), focused the flow of these high-temperature, sulfur-rich (and ^{34}S-enriched) fluids (Fig. 8a). Though, the studied samples were more likely near such a fault zone rather than within it because euhedral pyrites formed within serpentine (Fig. 4a–c) rather than within talc-chlorite-rich lithologies such as those observed in detachment faults along the Mid-Atlantic Ridge (Boschi et al., 2006a).

Subsequent uplift of the peridotite and further exposure of the mantle rock to seawater most likely changed fluid pathways and restricted their circulation, resulting in relatively reducing conditions (Fig. 8b). Temperatures of <~120 °C (Takai et al., 2008) and the reducing conditions imposed by progressive serpentinization permitted microbial activity and precipitation of the pyrrhotite ± pentlandite hosted in carbonate veins (Fig. 8b, area 2). Partial dissolution of first generation pyrite and replace-

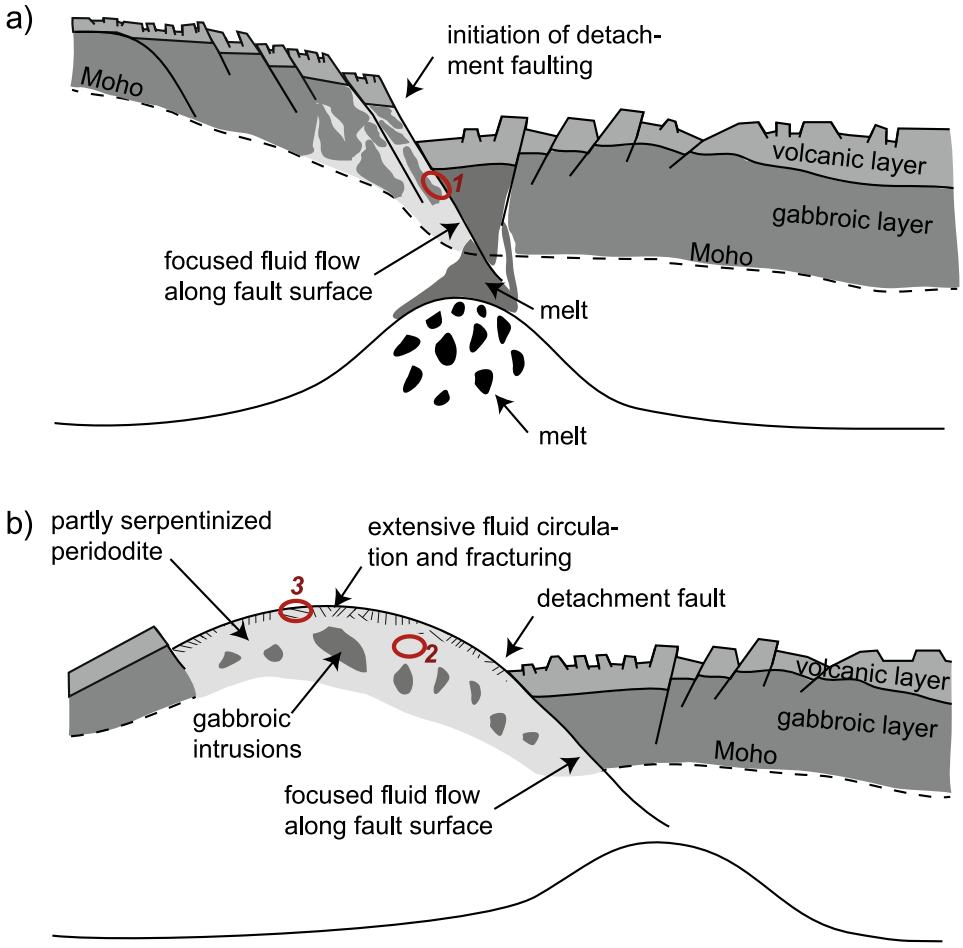

Fig. 8. Schematic evolution of the peridotite-hosted system in the N. Apennine with (a) initial formation of a detachment fault and (b) continuous exposure of mantle rock associated with the development of a core complex as typically observed along ultra-slow to slow-spreading mid-ocean ridges (Boschi et al., 2006b; Cannat et al., 2006; Ildefonse et al., 2007). The red ellipsoids describe the area of sulfide formation as suggested by the sulfide mineralogy and *in situ* isotope compositions: (1) Introduction of a high-temperature fluid and TSR to produce pyrite with $\delta^{34}S$ up to +16.1‰; (2) Uplift and continuous exposure of the peridotite with interaction of more reducing and low-temperature fluids that facilitate MSR to produce pyrrhotite and pentlandite with $\delta^{34}S$ as low as −33.7‰ that are hosted in calcite veins; (3) Extensive fracturing and introduction of more oxidizing fluids leading to pyrite formation with $\delta^{34}S$ values as low as −9.6‰. (For interpretation of the references to color in this figure legend, the reader is referred to the web version of this article.)

ment by pyrrhotite (or pentlandite) during this stage is documented by distinct mineral textures (Fig. 4c and d). Finally, later extensive fracturing and introduction of more volumes of oxidizing seawater resulted in extensive carbonate mineral precipitation and the formation of pyrite with negative $\delta^{34}S$ values, i.e., sulfide that was partially derived from MSR (Fig. 8b, area 3).

The evolution of the system from more reducing to more oxidizing agrees with the gradual cooling of the fluids from around 150 °C to 50 °C associated with progressive opening of fluid pathways as recorded in various generations of carbonate veins (Schwarzenbach et al., 2013). This last stage of water-rock interaction was associated with oxidation of sulfide minerals, the pseudomorphic replacement of pyrite by hematite and extensive water-rock interaction caused a loss of sulfide from the rocks (Schwarzenbach et al., 2012).

5.5. Constraints on the evolution of other peridotite-hosted hydrothermal systems

The comparison between bulk rock data and *in situ* sulfide analyses of the ODP and ophiolite samples document the complex hydrothermal evolution of peridotite-hosted hydrothermal systems with variable influence of high and low temperature processes. Similar to the N. Apennine, the investigated samples from ODP Site 1268 have a larger range in *in situ* $\delta^{34}S_{sulfide}$ (−12.1 to +14.7‰) than bulk rock $\delta^{34}S_{sulfide}$ analyses (4.1–10.8‰) observed in this and previous studies (Alt et al., 2007). Negative $\delta^{34}S$ from pyrite suggest that MSR took place at Site 1268 (Fig. 4k). This pyrite often displays corrosion features or rounded grains and it typically occurs within carbonate veins. This suggests that at Site 1268 MSR pre-dated introduction of high-temperature fluids (as also indicated by the mineralogy;

Bach et al., 2004), and that the biogenic isotopic signature is obscured in the bulk $\delta^{34}S$ and $\Delta^{33}S$ compositions.

In contrast, at the Iberian Margin the $\Delta^{33}S_{sulfide}$ reflects a dominance of MSR as discussed previously by Ono et al. (2012). In contrast to Ono et al. (2012), we separately determined the $\Delta^{33}S_{sulfide}$ of AVS and CRS fraction. The distinction between AVS and CRS fraction mostly reflects changes in the redox conditions, with AVS representing more reducing phases such as pyrrhotite and CRS representing comparatively more oxidizing phases such as pyrite. At Site 897 the CRS is dominant in the upper sections of the drill core while AVS is dominant in the lower part, which correlates with mineralogical observations (Alt and Shanks, 1998) and with the dominant species having more negative values (see supplementary Table S1). At Site 1070 the AVS fraction is dominant throughout the sequence and has $\delta^{34}S_{sulfide}$ values as low as −44.0‰. This is most likely due to a hypersulfidic environment where electron acceptors are limiting and sulfate reduction may take place without additional sulfur disproportionation (Brunner and Bernasconi, 2005; Wortmann et al., 2001).

6. SUMMARY AND CONCLUDING REMARKS

Using multiple sulfur isotopes, *in situ* sulfide analyses and petrographic observations we provide new and more detailed insight into sulfur cycling during the evolution of ancient peridotite-hosted hydrothermal systems. In particular, the serpentinites in the N. Apennine preserve a successive evolution of high-temperature water-rock interaction dominated by TSR in a closed system to low-temperature water-rock interaction that facilitated microbial activity. This evolution most likely coincided with the continuous uplift and exposure of the mantle rock to seawater during the tectonic history of this sequence. In contrast, the Santa Elena peridotites are dominated by high-temperature processes: closed system TSR was associated with the input of variable amounts of H_2S from black-smoker type fluids. This resulted in unusually positive $\delta^{34}S$ and $\Delta^{33}S$ signatures in sulfides and the formation of Cu-rich sulfide and metal mineral assemblages. In both systems, the model calculations require relatively high SO_4 contents in the initial fluid. We ascribe this to restricted anhydrite formation prior to TSR due to low Ca^{2+} concentrations in the serpentinizing fluids, either caused by calcium carbonate precipitation during initial fluid influx or because ultramafic rocks simply have lower CaO contents compared to mafic lithologies that may be released to the fluids. Effectively, the correlation between low Ca^{2+} concentrations in the fluid and limited SO_4 removal may play a significant role in providing SO_4 to the subsurface biosphere of peridotite-hosted hydrothermal systems, in particular for sulfate-reducing microbes that are found in these systems (e.g., Brazelton et al., 2006; Lang et al., 2012; Schrenk et al., 2013).

The interpretations drawn from the model calculations performed here compare well with previous studies (e.g., Alt et al., 2007; Ono et al., 2012). Though, we emphasize that the hydrothermal history of peridotite-hosted systems cannot always be resolved using bulk rock $\delta^{34}S$ and $\Delta^{33}S$ alone due to the complex histories that characterize these systems and involvement of several phases of sulfur cycling and resulting sulfur mineralogies. To provide a more detailed view of the processes that affect the sulfur geochemistry, *in situ* isotopic measurements can provide a useful tool when complimented with detailed petrographic and mineralogical observations.

In conclusion, temperature plays an important controlling role on the processes involved in the sulfur cycle during the alteration of ultramafic oceanic lithosphere. The studied systems show that they can evolve from high temperatures, where the sulfur cycling is dominated by TSR and input of gabbro-derived fluids, to lower temperatures that permit microbial activity, and vice versa. Importantly, this complex evolution can be preserved in a single hand sample. Overall, the combination of *in situ* and bulk rock multiple sulfur isotope analyses provides us with a more comprehensive view of the different episodes of hydrothermal circulation and the temporal dominance between biogenic and abiogenic processes that signify these systems. This is particularly beneficial when reconstructing the alteration history of serpentinites preserved in sequences of obducted, ancient oceanic lithosphere that have complex geologic histories.

ACKNOWLEDGEMENTS

We would like to thank Brian Monteleone for analyses of the SIMS sections at the Northeast National Ion Microprobe Facility (NENIMF). NENIMF gratefully acknowledges support from the National Science Foundation Instrumentation and Facilities Program, Division of Earth Sciences, and from The Woods Hole Oceanographic Institution. We also thank Erin Beirne for help during multiple sulfur analyses, Matthew Petroff and Ryan Ordung for assistance during sample preparation. We thank E. Gazel and J. Snow for providing the samples of the Santa Elena ophiolite. Careful and constructive reviews by J. Alt, D. Syverson and two anonymous reviewers are greatly acknowledged. This research used samples supplied by the Ocean Drilling Program (ODP). ODP is sponsored by the US National Science Foundation (NSF) and participating countries under management of Joint Oceanographic Institutions (JOI), Inc. This project was supported by NSF grant EAR 1324566 and C-DEBI grant OCE-0939564.

APPENDIX A. SUPPLEMENTARY MATERIAL

Supplementary data associated with this article can be found, in the online version, at https://doi.org/10.1016/j.gca.2017.12.006.

REFERENCES

Abbate E., Bortolotti V. and Principi G. (1980) Apennine ophiolites: a peculiar oceanic crust. *Ofioliti, Spec. Iss. Tethyan Ophiolites* **1**, 59–96.

Agrinier P. and Cannat M. (1997) Oxygen-isotope constraints on serpentinization processes in ultramafic rocks from the mid-atlantic ridge (23°N). *Proc. Ocean Drill. Program. Sci. Results* **153**, 381–388.

Alt J. C. and Shanks W. C. I. (1998) Sulfur in serpentinized oceanic peridotites: serpentinization processes and microbial sulfate reduction. *J. Geophys. Res.* **103**, 9917–9929.

Alt J. C. and Shanks W. C. I. (2003) Serpentinization of abyssal peridotites from the MARK area, Mid-Atlantic Ridge: sulfur geochemistry and reaction modeling. *Geochim. Cosmochim.* **67**, 641–653.

Alt J. C., Shanks W. C., Bach W., Paulick H., Garrido C. J. and Beaudoin G. (2007) Hydrothermal alteration and microbial sulfate reduction in peridotite and gabbro exposed by detachment faulting at the Mid-Atlantic Ridge, 15°20′N (ODP Leg 209): a sulfur and oxygen isotope study. *Geochem. Geophys.* **8**.

Alt J. C., Shanks, III, W. C., Crispini L., Gaggero L., Schwarzenbach E. M., Früh-Green G. L. and Bernasconi S. M. (2012) Uptake of carbon and sulfur during seafloor serpentinization and the effects of subduction metamorphism in Ligurian peridotites. *Chem. Geol.* **322–323**, 268–277.

Alt J. C., Schwarzenbach E. M., Früh-Green G. L., Shanks, III, W. C., Bernasconi S. M., Garrido C. J., Crispini L., Gaggero L., Padrón-Navarta J. A. and Marchesi C. (2013) The role of serpentinites in cycling of carbon and sulfur: seafloor serpentinization and subduction metamorphism. *Lithos* **178**, 40–54.

Andreani M., Mevel C., Boullier A. M. and Escartin J. (2007) Dynamic control on serpentine crystallization in veins: constraints on hydration processes in oceanic peridotites. *Geochem. Geophys.* **8**. https://doi.org/10.1029/2006gc001373, Q02012.

Bach W. and Humphris S. E. (1999) Relationship between the Sr and O isotope compositions of hydrothermal fluids and the spreading and magma-supply rates at oceanic spreading centers. *Geology* **27**, 1067–1070.

Bach W., Garrido C. J., Paulick H., Harvey J. and Rosner M. (2004) Seawater-peridotite interactions: first insights form ODP Leg 209, MAR 15°N. *Geochem. Geophys.* **5**, 22.

Bach W., Paulick H., Garrido C. J., Ildefonse B., Meurer W. P. and Humphris S. E. (2006) Unraveling the sequence of serpentinization reactions: petrography, mineral chemistry, and petrophysics of serpentinites from MAR 15°N (ODP Leg 209, Site 1274). *Geophys. Res. Lett.* **33**.

Barrett T. J. and Friedrichsen H. (1989) Stable isotopic composition of atypical ophiolites from East Liguria, Italy. *Chem. Geol.* **80**, 71–84.

Beard J. S., Frost B. R., Fryer P., McCaig A. M., Searle R. C., Ildefonse B., Zinin P. and Sharma S. K. (2009) Onset and progression of serpentinization and magnetite formation in olivine-rich troctolite from IODP Hole U1309D. *J. Petrol.* **50**, 387–403.

Boillot G., Grimaud S., Mauffret A., Mougenot D., Kornprobst J., Mergoil-Daniel J. and Torrent G. (1980) Ocean-continent boundary off the Iberian margin: a serpentinite diapir west of the Galicia Bank. *Earth Planet. Sci. Lett.* **48**, 23–34.

Boschi C., Früh-Green G. L., Delacour A., Karson J. A. and Kelley D. S. (2006a) Mass transfer and fluid flow during detachment faulting and development of an oceanic core complex, Atlantis Massif (MAR 30°). *Geochem. Geophys.* **7**.

Boschi C., Früh-Green G. L. and Escartin J. (2006b) Occurrence and significance of serpentinite-hosted, talc- and amphibole-rich fault rocks in modern oceanic settings and ophiolite complexes: an overview. *Ofioliti* **31**, 129–140.

Boschi C., Dini A., Früh-Green G. L. and Kelley D. S. (2008) Isotopic and element exchange during serpentinization and metasomatism at the Atlantis Massif (MAR 30°N): Insights from B and Sr isotope data. *Geochim. Cosmochim.* **72**, 1801–1823.

Brazelton W. J., Schrenk M. O., Kelley D. S. and Baross J. A. (2006) Methane- and sulfur-metabolizing microbial communities dominate the Lost City hydrothermal field ecosystem. *Appl. Environ.* **72**, 6257–6270.

Brazelton W. J., Mehta M. P., Kelley D. S. and Baross J. A. (2011) Physiological differentiation within a single-species biofilm fueled by serpentinization. *Mbio* **2**.

Brunner B. and Bernasconi S. M. (2005) A revised isotope fractionation model for dissimilatory sulfate reduction in sulfate reducing bacteria. *Geochim. Cosmochim.* **69**, 4759–4771.

Canfield D. E., Raiswell R., Westrich J. T., Reaves C. M. and Berner R. A. (1986) The use of chromium reduction in the analysis of reduced inorganic sulfur in sediments and shales. *Chem. Geol.* **54**, 149–155.

Cannat M. (1993) Emplacement of mantle rocks in the sea-floor at mid-ocean ridges. *J. Geophys. Res.* **98**, 4163–4172.

Cannat M., Sauter D., Mendel V., Ruellan E., Okino K., Escartin J., Combier V. and Baala M. (2006) Modes of seafloor generation at a melt-poor ultraslow-spreading ridge. *Geology* **34**, 605–608.

Casey J. F., Banerji D. and Zarian P. (2007) Leg 179 synthesis: geochemistry, stratigraphy, and structure of gabbroic rocks drilled in ODP Hole 1105A, Southwest Indian Ridge. In *Proc. Ocean Drill. Program, Sci. Results, College Station, TX* (eds. J. F. Casey and D. J. Miller), pp. 1–125.

Charlou J. L., Donval J. P., Fouquet Y., Jean-Baptiste P. and Holm N. (2002) Geochemistry of high H_2 and CH_4 vent fluids issuing from ultramafic rocks at the Rainbow hydrothermal field (36°14′N, MAR). *Chem. Geol.* **191**, 345–359.

Christensen P. R., McSween H. Y., Bandfield J. L., Ruff S. W., Rogers A. D., Hamilton V. E., Gorelick N., Wyatt M. B., Jakosky B. M., Kieffer H. H., Malin M. C. and Moersch J. E. (2005) Evidence for magmatic evolution and diversity on Mars from infrared observations. *Nature* **436**, 504–509.

Coplen T. B. and Krouse H. R. (1998) Sulphur isotope data consistency improved. *Nature* **392**, pp. 32-32.

Crowe D. E. and Vaughan R. G. (1996) Characterization and use of isotopically homogeneous standards for in situ laser microprobe analysis of $^{34}S/^{32}S$ ratios. *Am. Miner.* **81**, 187–193.

Delacour A., Früh-Green G. L. and Bernasconi S. M. (2008a) Sulfur mineralogy and geochemistry of serpentinites and gabbros of the Atlantis Massif (IODP Site U1309). *Geochim. Cosmochim.* **72**, 5111–5127.

Delacour A., Früh-Green G. L., Bernasconi S. M. and Kelley D. S. (2008b) Sulfur in peridotites and gabbros at Lost City (30°N, MAR): implications for hydrothermal alteration and microbial activity during serpentinization. *Geochim. Cosmochim.* **72**, 5090–5110.

Dick H. J. B., Lin J. and Schouten H. (2003) An ultraslow-spreading class of ocean ridge. *Nature* **426**, 405–412.

Ding T., Valkiers S., Kipphardt H., De Bièvre P., Taylor P. D. P., Gonfiantini R. and Krouse R. (2001) Calibrated sulfur isotope abundance ratios of three IAEA sulfur isotope reference materials and V-CDT with a reassessment of the atomic weight of sulfur. *Geochim. Cosmochim.* **65**, 2433–2437.

Douville E., Charlou J. L., Oelkers E. H., Bienvenu P., Jove Colon C. F., Donval J. P., Fouquet Y., Prieur D. and Appriou P. (2002) The Rainbow vent fluids (36°14′N, MAR): the influence of ultramafic rocks and phase separation on trace metal content in Mid-Atlantic Ridge hydrothermal fluids. *Chem. Geol.* **184**, 37–48.

Escartin J., Hirth G. and Evans B. (1997) Effects of serpentinization on the lithospheric strength and the style of normal faulting at slow-spreading ridges. *Earth Planet. Sci. Lett.* **151**, 181–189.

Escartin J., Hirth G. and Evans B. (2001) Strength of slightly serpentinized peridotites: implications for the tectonics of oceanic lithosphere. *Geology* **29**, 1023–1026.

Escuder-Viruete J., Baumgartner P. O. and Castillo-Carrión M. (2015) Compositional diversity in peridotites as result of a multi-process history: the Pacific-derived Santa Elena ophiolite, northwest Costa Rica. *Lithos* **231**, 16–34.

Farquhar J., Bao H. and Thiemens M. (2000a) Atmospheric influence of Earth's earliest sulfur cycle. *Science* **289**, 756–758.

Farquhar J., Jackson T. L. and Thiemens M. H. (2000b) A ^{33}S enrichment in ureilite meteorites: evidence for a nebular sulfur component. *Geochim. Cosmochim. Acta* **64**, 1819–1825.

Farquhar J., Savorino J., Jackson T. L. and Thiemens M. H. (2000c) Evidence of atmospheric sulphur in the martian regolith from sulphur isotopes in meteorites. *Nature* **404**, 50–52.

Farquhar J., Johnston D. T., Wing B. A., Habicht K. S., Canfield D. E., Airieau S. and Thiemens M. H. (2003) Multiple sulphur isotopic interpretations of biosynthetic pathways: implications for biological signatures in the sulphur isotope record. *Geobiology* **1**, 27–36.

Frost B. R. (1985) On the stability of sulfides, oxides, and native metals in serpentinite. *J. Petrol.* **26**, 31–63.

Frost B. R. and Beard J. S. (2007) On silica activity and serpentinization. *J. Petrol.* **48**, 1351–1368.

Fry B., Ruf W., Gest H. and Hayes J. M. (1988) Sulfur isotope effects associated with oxidation of sulfide by O_2 in aqueous solution. *Chem. Geol.* **73**, 205–210.

Früh-Green G. L., Plas A. and Lécuyer C. (1996) Petrologic and stable isotope constraints on hydrothermal alteration and serpentinization of the EPR shallow mantle at Hess Deep (Site 895). *Proc. Ocean Drill. Program, Sci. Results* **147**, 255–291.

Früh-Green G. L., Connolly J. A., Plas A., Kelley D. S. and Grobéty B. (2004) Serpentinization of oceanic peridotites: Implications for geochemical cycles and biological activity. In *The Subseafloor Biospere at Mid-Ocean Ridges*. American Geophysical Union, Washington, DC.

Garuti G., Bartoli O., Scacchetti M. and Zaccarini F. (2008) Geological setting and structural styles of Volcanic Massive Sulfide deposits in the northern Apennines (Italy): evidence for seafloor and sub-seafloor hydrothermal activity in unconventional ophiolites of the Mesozoic Tethys. *Boletin de la Sociedad Geologica Mexicana* **60**, 121–145.

German C. R., Petersen S. and Hannington M. D. (2016) Hydrothermal exploration of mid-ocean ridges: where might the largest sulfide deposits be forming? *Chem. Geol.* **420**, 114–126.

Halas S. and Szaran J. (2001) Improved thermal decomposition of sulfates to SO_2 and mass spectrometric determinations of $\delta^{34}S$ of IAEA-SO-5, IAEA-SO-6 and NBS-127 sulfate standards. *Rapid Commun. Mass Spectrom* **15**, 1618–1620.

Hardie L. A. (1996) Secular variation in seawater chemistry: An explanation for the coupled secular variation in the mineralogies of marine limestones and potash evaporites over the past 600 my. *Geology* **24**, 279–283.

Harvey J., Savov I. P., Agostini S., Cliff R. A. and Walshaw R. (2014) Si-metasomatism in serpentinized peridotite: the effects of talc-alteration on strontium and boron isotopes in abyssal serpentinites from Hole 1268a, ODP Leg 209. *Geochim. Cosmochim.* **126**, 30–48.

Horita J., Zimmermann H. and Holland H. D. (2002) Chemical evolution of seawater during the Phanerozoic: implications from the record of marine evaporites. *Geochim. Cosmochim.* **66**, 3733–3756.

Ildefonse B., Blackman D. K., John B. E., Ohara Y., Miller D. J. and MacLeod C. J. (2007) Oceanic core complexes and crustal accretion at slow-spreading ridges. *Geology* **35**, 623–626.

Johnston D. T. (2011) Multiple sulfur isotopes and the evolution of Earth's surface sulfur cycle. *Earth-Sci. Rev.* **106**, 161–183.

Johnston D. T., Farquhar J., Wing B. A., Kaufman A., Canfield D. E. and Habicht K. S. (2005) Multiple sulfur isotope fractionations in biological systems: a case study with sulfate reducers and sulfur disproportionators. *Am. J. Sci* **305**, 645–660.

Johnston D. T., Farquhar J. and Canfield D. (2007) Sulfur isotope insights into microbial sulfate reduction: when microbes meet models. *Geochim. Cosmochim.* **71**, 3929–3947.

Johnston D. T., Gill B. C., Masterson A., Beirne E., Casciotti K. L., Knapp A. N. and Berelson W. (2014) Placing an upper limit on cryptic marine sulphur cycling. *Nature* **513**, 530.

Kampschulte A. and Strauss H. (2004) The sulfur isotopic evolution of Phanerozoic seawater based on the analysis of structurally substituted sulfate in carbonates. *Chem. Geol.* **204**, 255–286.

Kelemen P., Kikawa E., Miller D.J. and shipboard scientific party (2007) Leg 209 summary. In Proc. Ocean Drill. Program, Ini. Results 209, College Station, TX.

Kelley S. D., Karson J. A., Blackman D. K., Früh-Green G. L., Butterfield D. A., Lilley D. M., Olson E. J., Schrenk M. O., Roell K. K., Lebon G. T. and Rivizzigno P.the AT3-60 Shipboard Party (2001) An off-axis hydrothermal vent field near the Mid-Atlantic Ridge at 30°N. *Nature* **412**, 145–149.

Kelley D. S., Karson J. A., Früh-Green G. L., Yoerger D. R., Shank T. M., Butterfield D. A., Hayes J. M., Schrenk M. O., Olson E. J., Proskurowski G., Jakuba M., Bradley A., Larson B., Ludwig K. A., Glickson D., Buckman K., Bradley A. S., Brazelton W. J., Roe K., Elend M. J., Delacour A., Bernasconi S. M., Lilley D. M., Baross J. A., Summons R. E. and Sylva S. P. (2005) A serpentinite-hosted ecosystem: the lost city hydrothermal field. *Science* **307**, 1428–1434.

Klein F. and Bach W. (2009) Fe-Ni-Co-O-S phase relations in peridotite-seawater interactions. *J. Petrol.* **50**, 37–59.

Klein F., Humphris S., Guo W., Schubotz F., Schwarzenbach E. M. and Orsi W. (2015) Fluid mixing and the deep biosphere of a fossil Lost City-type hydrothermal system at the Iberian Margin. *PNAS* **112**, 12036–12041.

Labidi J., Cartigny P., Birck J. L., Assayag N. and Bourrand J. J. (2012) Determination of multiple sulfur isotopes in glasses: a reappraisal of the MORB $\delta^{34}S$. *Chem. Geol.* **334**, 189–198.

Labidi J., Shahar A., Le Losq C., Hillgren V. J., Mysen B. O. and Farquhar J. (2016) Experimentally determined sulfur isotope fractionation between metal and silicate and implications for planetary differentiation. *Geochim. Cosmochim.* **175**, 181–194.

Lackschewitz K.S., Armini M., Augustin N., Dubilier N., Edge D., Engemann G., Fabian M., Felden J., Franke P., Gärtner A., Garbe-Schönberg D., Gennerich H.-H., Hüttig D., Marbler H., Meyerdierks A., Pape T., Perner M., Reuter M., Ruhland G., Schmidt, K., Schott T., Schroeder M., Schroll G., Seiter C., Stecher J., Strauss H., Viehweger M., Weber S., Wenzhöfer F. and Zielinski F. (2005) Longterm study of hydrothermalism and biology at the Logatchev field, Mid-Atlantic Ridge at 14° 45′N (revisit 2005; HYDROMAR II). Cruise Report.

Lagabrielle Y. and Cannat M. (1990) Alpine Jurassic ophiolites resemble the modern central Atlantic basement. *Geology* **18**, 319–322.

Lang S. Q., Früh-Green G. L., Bernasconi S. M., Lilley M. D., Proskurowski G., Méhay S. and Butterfield D. A. (2012) Microbial utilization of abiogenic carbon and hydrogen in a serpentinite-hosted system. *Geochim. Cosmochim.* **92**, 82–99.

Lemoine M. (1980) Serpentinites, gabbros and ophicalcites in the Piemont-Ligurian domain of the western Alps - possible indicators of oceanic fracture-zones and of associated serpentinite protrusions in the Jurassic-Cretaceous Tethys. *Arch. Sci.* **33**, 103–115.

Lorand J. P. (1989a) Abundance and distribution of Cu-Fe-Ni sulfides, sulfur, copper and platinum-group elements in oro-

genic-type spinel lherzolite massifs of Ariäge (northeastern Pyrenees, France). *Earth Planet. Sci. Lett.* **93**, 50–64.

Lorand J. P. (1989b) Mineralogy and chemistry of Cu-Fe-Ni sulfides in orogenic-type spinel peridoite bodies from Ariege (Northeastern Pyrenees, France). *Contrib. Mineral.* **103**, 335–345.

Lorand J.-P. (1991) Sulphide petrology and sulphur geochemistry of orogenic lherzolites: a comparative study of the Pyrenean bodies (France) and the Lanzo Massif (Italy). *J. Petrol. Special*, 77–95.

Madrigal P., Gazel E., Denyer P., Smith I., Jicha B., Flores K., Coleman D. and Snow J. (2015) A melt-focusing zone in the lithospheric mantle preserved in the Santa Elena Ophiolite, Costa Rica. Lithos.

Masterson A. (2016) Multiple sulfur isotope applications in diagenetic models and geochemical proxy records. Department of Earth and planetary Sciences, Harvard University, Cambridge, Massachusetts. p. 175.

Masterson A. L., Wing B. A., Paytan A., Farquhar J. and Johnston D. T. (2016) The minor sulfur isotope composition of Cretaceous and Cenozoic seawater sulfate. *Paleoceanography* **31**.

McCaig A. M., Cliff R. A., Escartin J., Fallick A. E. and MacLeod C. J. (2007) Oceanic detachment faults focus very large volumes of black smoker fluids. *Geology* **35**, 935–938.

McDermott J. M., Ono S., Tivey M. K., Seewald J. S., Shanks W. C. and Solow A. R. (2015) Identification of sulfur sources and isotopic equilibria in submarine hot-springs using multiple sulfur isotopes. *Geochim. Cosmochim.* **160**, 169–187.

Moody J. B. (1976) Serpentinization - review. *Lithos* **9**, 125–138.

Oeser M., Strauss H., Wolff P. E., Koepke J., Peters M., Garbe-Schönberg D. and Dietrich M. (2012) A profile of multiple sulfur isotopes through the Oman ophiolite. *Chem. Geol.* **312–313**, 27–46.

Ohmoto H. and Rye R. O. (1979) Isotopes of sulfur and carbon. In *Geochemistry of Hydrothermal Ore Deposits* (ed. H. L. Barnes), second ed. Wiley, New York, pp. 509–567.

Ohmoto H. and Lasaga A. C. (1982) Kinetics of reactions between aqueous sulfates and sulfides in hydrothermal systems. *Geochim. Cosmochim. Acta* **46**, 1727–1745.

Ono S., Eigenbrode J. L., Pavlov A. A., Pushker K., Rumble D., Kasting J. F. and Freeman K. H. (2003) New insights into Archean sulfur cycle from mass-independent sulfur isotope records from the Hamersley Basin, Australia. *Earth Planet. Sci. Lett.* **213**, 15–30.

Ono S., Wing B., Johnston D., Farquhar J. and Rumble D. (2006) Mass-dependent fractionation of quadruple stable sulfur isotope system as a new tracer of sulfur biogeochemical cycles. *Geochim. Cosmochim. Acta* **70**, 2238–2252.

Ono S., Shanks W. C. I., Rouxel O. J. and Rumble D. (2007) S-33 constraints on the seawater sulfate contribution in modern seafloor hydrothermal vent sulfides. *Geochim. Cosmochim.* **71**, 1170–1182.

Ono S., Keller N. S., Rouxel O. and Alt J. C. (2012) Sulfur-33 constraints on the origin of secondary pyrite in altered oceanic basement. *Geochim. Cosmochim. Acta* **87**, 323–340.

Paulick H., Bach W., Godard M., De Hoog J. C. M., Suhr G. and Harvey J. (2006) Geochemistry of abyssal peridotites (Mid-Atlantic Ridge, 15°20′N, ODP Leg 209): Implications for fluid/rock interaction in slow spreading environments. *Chem. Geol.* **234**, 179–210.

Paytan A., Kastner M., Campbell D. and Thiemens M. H. (2004) Seawater sulfur isotope fluctuations in the Cretaceous. *Science* **304**, 1663–1665.

Peters M., Strauss H., Farquhar J., Ockert C., Eickmann B. and Jost C. L. (2010) Sulfur cycling at the Mid-Atlantic Ridge: a multiple sulfur isotope approach. *Chem. Geol.* **269**, 180–196.

Peters M., Strauss H., Petersen S., Kummer N.-A. and Thomazo C. (2011) Hydrothermalism in the Tyrrhenian Sea: inorganic and microbial sulfur cycling as revealed by geochemical and multiple sulfur isotope data. *Chem. Geol.* **280**, 217–231.

Petersen S., Kuhn K., Kuhn T., Augustin N., Hekinian R., Franz L. and Borowski C. (2009) The geological setting of the ultramafic-hosted Logatchev hydrothermal field (14°45′N, Mid-Atlantic Ridge) and its influence on massive sulfide formation. *Lithos* **112**, 40–56.

Proskurowski G., Lilley M., Seewald J., Früh-Green G. L., Olson E. J., Lupton J. E., Sylva S. P. and Kelley D. S. (2008) Abiogenic hydrocarbon production at Lost City hydrothermal field. *Science* **319**, 604–607.

Rees C. E. (1973) A steady-state model for sulphur isotope fractionation in bacterial reduction processes. *Geochim. Cosmochim.* **37**, 1141–1162.

Robinson B.W. (1995) Reference and intercomparison materials for stable isotopes of light elements. In Proceedings of a Consultants' Meeting Held in Vienna, 1–3, Dec. 1993. pp. 39–45.

Rouxel O., Ono S., Alt J., Rumble D. and Ludden J. (2008) Sulfur isotope evidence for microbial sulfate reduction in altered oceanic basalts at ODP Site 801. *Earth Planet. Sci. Lett.* **268**, 110–123.

Russell M. J., Hall A. J. and Martin W. (2010) Serpentinization as a source of energy at the origin of life. *Geobiology* **8**, 355–371.

Sakai H., Desmarais D. J., Ueda A. and Moore J. G. (1984) Concentrations and isotope ratios of carbon, nitrogen and sulfur in ocean-floor basalts. *Geochim. Cosmochim.* **48**, 2433–2441.

Salters V. J. M. and Stracke A. (2004) Composition of the depleted mantle. *Geochem. Geophys.* **5**, 1–27.

Sanchez-Murillo R., Gazel E., Schwarzenbach E. M., Crespo-Medina M., Schrenk M. O., Boll J. and Gill B. C. (2014) Geochemical evidence for active tropical serpentinization in the Santa Elena Ophiolite, Costa Rica: an analog of a humid early Earth? *Geochem. Geophys.* **15**, 1783–1800.

Sawyer D.S., Whitmarsh R.B., Klaus A., et al. (1994) Iberia Abyssal Plain Sites 897-901. In Proc. Ocean Drill. Program, Ini. Reports, College Station, TX.

Schmidt K., Koschinsky A., Garbe-Schonberg D., de Carvalho L. M. and Seifert R. (2007) Geochemistry of hydrothermal fluids from the ultramafic-hosted Logatchev hydrothermal field, 15 degrees N on the Mid-Atlantic Ridge: temporal and spatial investigation. *Chem. Geol.* **242**, 1–21.

Schrenk M. O., Kelley D. S., Bolton S. A. and Barossa J. A. (2004) Low archaeal diversity linked to subseafloor geochemical processes at the Lost City Hydrothermal Field, Mid-Atlantic Ridge. *Environ. Microbiol.* **6**, 1086–1095.

Schrenk M. O., Brazelton W. J. and Lang S. Q. (2013) Serpentinization, carbon, and deep life. *Rev. Mineral. Geochem.* **75**, 575–606.

Schulte M., Blake D., Hoehler T. and McCollom T. (2006) Serpentinization and its implications for life on the early Earth and Mars. *Astrobiology* **6**, 364–376.

Schwarzenbach E.M. (2011) Serpentinization, fluids and life: Comparing carbon and sulfur cycles in modern and ancient environments. Department of Earth Sciences, ETH Zurich, Zurich,p. 240.

Schwarzenbach E. M., Früh-Green G. L., Bernasconi S. M., Alt J. C., Shanks, III, W. C., Gaggero L. and Crispini L. (2012) Sulfur geochemistry of peridotite-hosted hydrothermal systems: comparing the Ligurian ophiolites with oceanic serpentinites. *Geochim. Cosmochim.* **91**, 283–305.

Schwarzenbach E. M., Früh-Green G. L., Bernasconi S. M., Alt J. C. and Plas A. (2013) Serpentinization and carbon sequestra-

tion: a study of two ancient peridotite-hosted hydrothermal systems. *Chem. Geol.* **351**, 115–133.

Schwarzenbach E. M., Gazel E. and Caddick M. J. (2014) Hydrothermal processes in partially serpentinized peridotites from Costa Rica: evidence from native copper and complex sulfide assemblages. *Contrib. Mineral.* **168**, 1–21.

Schwarzenbach E. M., Caddick M. J., Beard J. S. and Bodnar R. J. (2016a) Serpentinization, element transfer, and the progressive development of zoning in veins: evidence from a partially serpentinized harzburgite. *Contrib. Mineral.* **171**, 1–22.

Schwarzenbach E. M., Gill B. C., Gazel E. and Madrigal P. (2016b) Sulfur and carbon geochemistry of the Santa Elena peridotites: comparing oceanic and continental processes during peridotite alteration. *Lithos* **252–253**, 92–108.

Seyfried J. W. E. and Bischoff J. L. (1981) Experimental seawater-basalt interaction at 300 °C, 500 bars, chemical exchange, secondary mineral formation and implications for the transport of heavy metals. *Geochim. Cosmochim. Acta* **45**, 135–147.

Shanks W.C. (2001) Stable isotopes in seafloor hydrothermal systems: Vent fluids. Hydrothermal deposits, hydrothermal alteration, and microbial processes. In Stable Isotope Geochemistry (eds. J.W. Valley, D.R. Cole). The Mineralogical Society of America, pp. 469–525.

Shanks W. C., Bischoff J. L. and Rosenbauer R. J. (1981) Seawater sulfate reduction and sulfur isotope fractionation in basaltic systems: interaction of seawater with fayalite and magnetite at 200–300 °C. *Geochim. Cosmochim. Acta* **45**, 1977–1995.

Shanks W. C., Böhlke J. K. and Seal R. R. (1995) Stable Isotopes in Mid-ocean Ridge Hydrothermal Systems: Interactions Between Fluids, Minerals, and Organisms. American Geophysical Union, Washington D.C.

Sim M. S., Bosak T. and Ono S. (2011) Large sulfur isotope fractionation does not require disproportionation. *Science* **333**, 74–77.

Snow J. E. and Dick H. J. B. (1995) Pervasive magnesium loss by marine weathering of peridotite. *Geochim. Cosmochim.* **59**, 4219–4235.

Stickler W., Gonfiantini R. and Rozanski K. (1995) Reference and intercomparison materials for stable isotopes of light elements. In Proceedings of a Consultants' Meeting Held in Vienna, 1–3, Dec. 1993, pp. 7–11.

Syverson D. D., Ono S., Shanks W. C. and Seyfried, Jr, W. E. (2015) Multiple sulfur isotope fractionation and mass transfer processes during pyrite precipitation and recrystallization: an experimental study at 300 and 350 C. *Geochim. Cosmochim.* **165**, 418–434.

Takai K., Nakamura K., Toki T., Tsunogai U., Miyazaki M., Miyazaki J., Hirayama H., Nakagawa S., Nunoura T. and Horikoshi K. (2008) Cell proliferation at 122 C and isotopically heavy CH_4 production by a hyperthermophilic methanogen under high-pressure cultivation. *PNAS* **105**, 10949–10954.

Timofeeff M. N., Lowenstein T. K., Da Silva M. A. M. and Harris N. B. (2006) Secular variation in the major-ion chemistry of seawater: evidence from fluid inclusions in Cretaceous halites. *Geochim. Cosmochim.* **70**, 1977–1994.

Tuttle M. L., Goldhaber M. B. and Williamson D. L. (1986) An analytical scheme for determining forms of sulfphur in oil shales and associated rocks. *Talanta* **33**, 953–961.

Ueno Y., Ono S., Rumble D. and Maruyama S. (2008) Quadruple sulfur isotope analysis of ca. 3.5 Ga Dresser Formation: new evidence for microbial sulfate reduction in the early Archean. *Geochim. Cosmochim.* **72**, 5675–5691.

Vance S. D., Hand K. P. and Pappalardo R. T. (2016) Geophysical controls of chemical disequilibria in Europa. *Geophys. Res. Lett.* **43**, 4871–4879.

von Damm K. L. (1990) Seafloor hydrothermal activity: black smoker chemistry and chimneys. *Annu. Rev. Earth* **18**, 173.

Whitmarsh R. B. and Wallace P. J. (2001) The rift-to-drift development of the West Iberia nonvolcanic continental margin: a summary and review of the contribution of ocean drilling programm Leg 173. *Proc. Ocean Drill. Program, Sci. Results* **173**, 1–36.

Whitmarsh R. B., Beslier M.-O., Wallace P. J. et al. (1998) Return to Iberia Sites 1065-1070. In Proc. Ocean Drill. Program, Ini. Reports, College Station, TX.

Wortmann U. G. and Paytan A. (2012) Rapid variability of seawater chemistry over the past 130 Million years. *Science* **337**, 334–337.

Wortmann U. G., Bernasconi S. M. and Bottcher M. E. (2001) Hypersulfidic deep biosphere indicates extreme sulfur isotope fractionation during single-step microbial sulfate reduction. *Geology* **29**, 647–650.

Associate editor: Jeffrey C. Alt